Numerical methods for multidimensional radiative transfer*

E. Meinköhn[1,2], G. Kanschat[1], R. Rannacher[1,3], and R. Wehrse[2,3]

[1] Institute of Applied Mathematics, University of Heidelberg,
[2] Institute for Theoretical Astrophysics, University of Heidelberg,
[3] Interdisciplinary Center for Scientific Computing, University of Heidelberg

1 Abstract

This paper presents a continuous finite element method for solving the resonance line transfer problem in moving media. The algorithm is capable of dealing with three spatial dimensions, using hierarchically structured grids which are locally refined by means of duality-based a-posteriori error estimates. Application of the method to coherent isotropic scattering and complete redistribution gives a result of matrix structure which is discussed in the paper. The solution is obtained by way of an iterative procedure, which solves a succession of quasi-monochromatic radiative transfer problems. It is therefore immediately evident that any simulation of the extended frequency-dependent model requires a solution strategy for the elementary monochromatic transfer problem, which is fast as well as accurate. The present implementation is applicable to arbitrary model configurations with optical depths up to 10^3–10^4. Additionally, a combination of a discontinuous finite element method with a superior preconditioning method is presented, which is designed to overcome the extremely poor convergence properties of the linear solver for optically thick and highly scattering media. The contents of this article is as follows:

- Introduction
- Overview: Numerical Methods
- Monochromatic 3D Radiative Transfer
- Polychromatic 3D Line Transfer
- Test Calculations
- Applications
- Multi-Model Preconditioning
- Summary
- References

*This work has been supported by the German Research Foundation (DFG) through SFB 359 (Project C2).

2 Introduction

Energy transfer via radiation plays a key role in various scientific applications, such as combustion physics, thermonuclear fusion and astrophysics. The equation describing the transport of photons or neutrons through a medium and thereby accounting for absorption and emission effects is generally known as radiative transfer equation or radiation transport equation. It takes the form of a partial integro-differential equation that turns out to be equivalent to a linear Boltzmann equation if certain simplifications can be made. These simplifications arise, for instance, from an a-priori knowledge of the temperature field or from the assumption of local thermodynamic equilibrium. But as soon as these simplifications are dropped, non-linearities occur by way of the extinction coefficients or opacities, which depend on the temperature or on the number density of the energy-level population.

In astrophysics, particularly, it is obvious that next to the sensitivity improvements of the telescope equipment in the 1980s the current telescope development is characterized by an extraordinary improvement in spatial resolution: of course, the positioning of telescopes on satellites in space is one factor for this improvement, but the main fact is the use of so-called new generation telescopes with their computer controlled active and adaptive optical components. Especially, in combining these new instruments to very powerful modern interferometers provide spatially excellent resolved observations, revealing the geometrical complexity of many celestial objects. Thus, numerical codes for spherical-symmetrical or plane-parallel geometry, commonly used for astrophysical applications for decades, are not sufficient anymore. Modeling these multidimensional transfer problems makes the use of codes exploiting at least the 2D – in many cases the full 3D – structure indispensable.

In this paper, a summary of a collaboration between the numerics division of the Institute of Applied Mathematics and the Institute for Theoretical Astrophysics, both part of the University of Heidelberg, is presented. This interdisciplinary project started more than a decade ago, resulting in a continuous finite element method for solving multidimensional resonance line transfer problems in moving media. The appearance of an emission line profile is predominantly determined by complex angle-frequency couplings and by the macroscopic velocity field. Thus, taking scattering and Doppler effects into consideration, the corresponding three-dimensional radiative transfer equation is a partial integro-differential equation for the invariant radiation intensity $\mathcal{I} = \mathcal{I}(\mathbf{x}, \mathbf{n}, \nu, t)$ (cf. [MW84]), depending on the spatial variable $\mathbf{x}$, photon propagation direction $\mathbf{n}$, frequency ν and time variable t:

$$\frac{1}{c}\frac{\partial}{\partial t}\mathcal{I} + \mathbf{n}\cdot\nabla_x\mathcal{I} \;-\; \frac{\nu}{1+\mathbf{n}\cdot\frac{\mathbf{v}}{c}}\,\mathbf{n}\cdot\nabla_x\left(\mathbf{n}\cdot\frac{\mathbf{v}}{c}\right)\frac{\partial\mathcal{I}}{\partial\nu} = \\ -\left(\kappa+\sigma\right)\mathcal{I} \;+\; \sigma\int\limits_{\mathbb{R}^+}\int\limits_{S^2} R\,\mathcal{I}\,d\hat{\omega}\,d\hat{\nu} + \kappa\,B. \tag{1}$$

The parameters entering this equation are:

$$
\begin{aligned}
S^2 &: \quad \text{unit sphere within } \mathbb{R}^3 \\
\omega &: \quad \text{solid angle} \\
c &: \quad \text{speed of light} \\
\mathbf{v} &: \quad \text{velocity field} \\
\kappa = \kappa(\mathbf{x}, \nu) &: \quad \text{absorption coefficient} \\
\sigma = \sigma(\mathbf{x}, \nu) &: \quad \text{scattering coefficient} \\
R = R(\hat{\nu}, \hat{\mathbf{n}}; \nu, \mathbf{n}) &: \quad \text{redistribution function} \\
B = B(\nu, T(\mathbf{x})) &: \quad \text{Planck function} \\
T(\mathbf{x}) &: \quad \text{temperature field}
\end{aligned}
$$

If we assume that the velocity field causes no change of sign of the Doppler term, i.e. the term including the frequency derivative, Eq. (1) is generally solved with the constraint that the initial values of both the time and the frequency variable are fixed, and that the intensity of the incident radiation originating from outside the spatial domain is a given function at the boundary. More complex velocity fields give rise to a frequency boundary value problem rather than an initial value problem.

The algorithm discussed here works in three spatial dimensions on hierarchically structured grids which are locally refined by means of duality-based a-posteriori error estimates ("DRW method"; see [BR01] and the articles [BBR05, BKM05, BR05a, BR05b, CHR05] in this volume). The solution is obtained using an iterative procedure, where quasi-monochromatic radiative transfer problems are solved successively. Thus, a fast and accurate solution strategy for the monochromatic transfer problem is crucial to simulate the extended frequency-dependent model efficiently (for more details see [Kan96, RM01, MR02, Mei02]). A detailed overview of recent numerical methods for multidimensional radiative transfer problems is given in Sect. 3. Section 4 provides a detailed description and solution strategy of the monochromatic 3D radiative transfer problem. In Sect. 5 an algorithm for the solution of the frequency-dependent line transfer problem is presented. The code accounts for arbitrary velocity fields up to approximately 10% of the speed of light and complete redistribution. The latter is critical, e.g., for the correct modeling of Lyα line profiles in optically thick media. A sample of test calculations for line transfer problems is presented in Sect. 6 illustrating the underlying physics. In Sect. 7 results for more complex multidimensional configurations are presented. Finally, in Sect. 8 a preconditioner for monochromatic radiative transfer problems is derived. It is based on a smoothing operator for specific intensities and on the diffusion approximation of the mean intensity. The scheme presented combines these two preconditioners in a way related to two-level multigrid algorithms. It is demonstrated that the method allows for fast solution of the discrete linear problems in optically thick media where scattering dominates as well as when transition layers occur.

3 Overview: Numerical Methods

The development of advanced discretization methods for the transport equation is of fundamental importance, since the numerical effort of modeling increasingly complex multidimensional problems with increasing accuracy is still extremely challenging:

- The radiation intensity is in general (neglecting polarization) a function of seven variables: three spatial variables $\mathbf{x} = (x, y, z)$, two angular variables describing the photon propagation direction $\mathbf{n}$, one frequency variable ν, and one time variable t. Even if only a moderate discretization of 10^2 grid points for each independent variable is taken into consideration, result in a huge discrete problem with 10^{14} unknowns. This amount of data demands not only extremely powerful computers, but also efficient numerical methods to reduce the memory and CPU requirements. Especially for the latter point, an appropriate discretization method is of fundamental importance.
- The intensity is usually a rapidly changing function of the spatial, angular and frequency variables yielding jumps of the intensity or its derivatives within small parts of the corresponding computational domain. These jumps usually cause a considerable loss in accuracy for many discretization methods.
- Depending on the coefficient ranges, the linear Boltzmann equation behaves like totally different equation types: in material free areas it behaves like a hyperbolic wave equation; in scattering dominant, optically thick media it behaves like an elliptic (steady-state) or parabolic (time-dependent) diffusion equation; and in regions with highly forward-peaked phase function, it can behave like a parabolic equation. It is extremely difficult to find a discretization method efficiently dealing with these different types of behavior.

Numerical algorithms solving multidimensional radiative transfer problems are described in numerous publications since the late 1980s. These algorithms may be roughly classified in three categories: Monte-Carlo methods, Discrete-Ordinate methods and Angle-Moment methods. The stochastic approach of *Monte-Carlo* codes is extremely flexible, since the concept of following photon packages is in principal applicable to arbitrary multidimensional configurations, as, e.g., to the ultraviolet continuum transfer [Spa96], the optical and infrared continuum transport [WHS99], the molecular line transfer [Hog98, Juv97, PH98], and the Compton scattering [PSS79, HM91]. If the optical depth of the configuration is not too large, Monte-Carlo methods converge reasonably fast. In the case of large optical depths, this method is usually extraordinarily time consuming. The latter case is, however, favorable for the deterministic *Angle-Moment* method, which usually assumes the so-called diffusion approximation [YBL93, SPY95, MCK94]. Unfortunately, this technique is not applicable within optically thin regions, where the diffusion approximation is not valid anymore and the radiation field may significantly deviate

from isotropy. Another deterministic approach to solve multidimensional radiative transfer problems, the *Discrete-Ordinate* method, is characterized by the additional discretization of the photon propagation direction. In order to avoid numerical artefacts, the subdivision of the ordinate domain has to be preferably uniform. The spatial discretization, i.e. the discretization of the transport operator of the radiative transfer equation, is often performed by using approaches based on finite differences [SSW91] or by using the method of characteristics [DT00].

These methods usually work on structured grids, yielding algebraic systems that are solved very fast for homogeneous media and smooth data, but fail in the case of complex geometries or steep gradients of the solution and coefficients. The resulting system is by far too large to be solved even on supercomputers, since very high resolution is needed to produce accurate solutions for the challenging configurations described above. For many radiative transfer problems the steep gradients of the coefficients or the solution is confined to small regions within the computational domain. Only these small parts need the high resolution and the rest of the spatial domain must be resolved moderately, since the transport of photons is smooth. Solution adapted, locally refined grids offer the possibility to achieve highly resolved small areas of rapidly changing solutions, whereas in regions of smooth transport the grid remains coarse. Unfortunately, the generation of adaptively refined grids on the basis of a finite difference or characteristics method is extremely difficult. Alternatively, the finite element method (FEM) is exceedingly suitable to deal with adaptively refined grids and, therefore, approximates complex geometries and steep gradients of the coefficients and of the solution very well. A FEM upwind discretization on pre-refined grids is presented in [Tur93]. In [Kan96] the FEM discretization is stabilized via the streamline diffusion method yielding locally refined and, therefore, problem adapted grids by means of duality-based a-posteriori error estimates ("DRW method"; for details see [BR01] and the articles [BBR05, BKM05, BR05a, BR05b, CHR05] in this volume). Despite its evident advantages, the FEM is rarely used up to now within the astronomical community, since the code development is more complex than for the other commonly used discretization methods described above.

The discretization of multidimensional radiative transfer problems yield extremely large linear systems of algebraic equations, making direct solution strategies impossible. Usually, an iterative scheme is applied to solve these large systems of equations (e.g., see [Hac93, Var00]). The standard iterative method used in astrophysics to solve these systems is the so-called Λ- or Source Iteration method [Mih78]. Considering the whole discrete system, it is a Richardson method with nearly block-Jacobi preconditioning. Using a full Jacobi preconditioner is a first step to better convergence rates [Tur93]. Since the transport operator is inverted explicitly, these methods converge extremely fast for transport dominated problems. Exploiting the triangular matrix structure of an upwind discretization, the inversion is indeed very cheap (one matrix-vector-multiplication). In the case of highly scattering, optically

Table 1. *A radiative transfer model hierarchy. For details see text below.*

Geometry	**Scattering**	**Motion**	**Thermodyn.**	**Time**
1D plane-parallel	none	none	LTE	stationary
1D spher.-symm.	coherent, isotropic	slow (v/c < 10%)	NLTE, 2-level	non-stationary level pop.
2D euclidian	coherent, non-isotropic	fast (v/c > 10%)	NLTE, multi-level	non-stationary radiation
3D euclidian	complete redistribution, isotropic		general distribution	
3D non-euclidian	partial redistribution, isotropic			
	partial redistribution, non-isotropic			

thick media this method – like other stationary iterations – breaks down, since the condition number of the iteration matrix becomes very large. Since the convergence rate of preconditioned Richardson iteration methods only depend on the condition number, these are not suited for the scattering dominated case. But here [Kan96] comes in handy, showing that the eigenvalue distribution of the transport matrix is clustered, with one of the eigenvalues vanishing whilst the others are either close to unity or at least bounded away from zero. Krylov space methods like GMRES or bi-CGSTAB (for details see [SF93] and references therein) are particular suitable to deal with this eigenvalue distribution [Kan96]. Being superior to stationary iteration methods, Krylov type solvers still show poor convergence properties for scattering dominant transfer problems, necessitating the use of convergence acceleration methods.

During the last several decades, significant progress has been achieved in the development of acceleration methods, i.e. preconditioning methods, for discrete-ordinate methods that sped up the iterative convergence of these problems. A comprehensive review article was recently published (see [AL02]), which covers practically all of the main methods that have been discussed above. When comparing the various acceleration methods, the Diffusion Synthetic Acceleration (DSA) turns out to be a very efficient preconditioning method guaranteeing rapid convergence for all values of optical depths and scattering coefficients. DSA exploits the diffusion approximation, a well-known approximation of the Boltzmann equation for highly scattering, optically thick media, so as to establish a solution of the full radiative transfer problem in a very efficient way. Preconditioning leads to acceleration in the discretized source iteration, which corresponds to a Richardson iteration, and the algorithm makes use of DSA efficiently as well as robustly. Discrete transport problems, for which a convergence in source iteration would ordinarily require

hundreds, thousands, or even millions of iteration steps, are now solved with DSA in less than a few tens iterations. Unfortunately, this method shows a loss in the effectiveness for multidimensional Cartesian grids in the presence of material discontinuities. In [WWM04] it is shown that a Krylov iterative method, preconditioned with DSA, is an effective remedy that can be used to efficiently compute solutions for this class of problems. Results from numerical experiments show that replacing source iteration with a preconditioned Krylov method can efficiently solve transfer problems that are virtually intractable with accelerated source iteration (see [WWM04]).

Next to Monte-Carlo and extremely slow Angle-Moment methods (see [SL87, ER90]), only the finite difference method described in [SSW91] existed prior to the Heidelberg project of developing a robust FEM code modeling multidimensional radiation fields in heterogeneous and highly scattering media. Table 1 displays a radiative transfer model hierarchy. The marked boxes correspond to the models the codes developed at Heidelberg University are able to deal with. The abbreviations LTE and NLTE account for local and non-local thermodynamic equilibrium, respectively.

4 Monochromatic 3D Radiative Transfer

4.1 The Radiative Transfer Problem

Our aim is the calculation of the radiation field in diffuse matter in space. Assuming the matter is surrounded by a vacuum, we will only consider a convex domain containing the area of interest. Radiation leaving this domain will not enter it again. Inside this 3D domain $\Omega \subset \mathbb{R}^3$, the specific intensity I satisfies the monochromatic radiative transfer equation

$$\begin{aligned} &\mathbf{n} \cdot \nabla_x I(\mathbf{x}, \mathbf{n}) + \kappa(\mathbf{x}) I(\mathbf{x}, \mathbf{n}) \\ &\qquad + \sigma(\mathbf{x}) \Big(I(\mathbf{x}, \mathbf{n}) - \frac{1}{4\pi} \int_{S^2} P(\mathbf{n}', \mathbf{n}) I(\mathbf{x}, \mathbf{n}') \, d\omega' \Big) = f(\mathbf{x}), \end{aligned} \tag{2}$$

where $\mathbf{x} \in \Omega$ is location in space and $\mathbf{n}$ is the unit vector pointing in the direction of the solid angle $d\omega$ of the unit sphere S^2. The optical properties of the matter are given by the absorption coefficient $\kappa(\mathbf{x})$ and the scattering coefficient $\sigma(\mathbf{x})$. The angular phase function P occurring in the scattering integral is normalized, such that $\frac{1}{4\pi} \int P(\mathbf{n}', \mathbf{n}) \, d\omega' = 1$. The source term

$$f(\mathbf{x}) = \kappa(\mathbf{x}) B(T(\mathbf{x})) + \epsilon(\mathbf{x}) \tag{3}$$

consists of thermal emission depending on a temperature distribution $T(\mathbf{x})$ and an additional emissivity $\epsilon(\mathbf{x})$ of a point source or an extended object. B is the Planck-Function. To be able to solve Eq. (2), boundary conditions of the form

$$I(\mathbf{x}, \mathbf{n}) = g(\mathbf{x}, \mathbf{n}) \tag{4}$$

must be imposed on the "inflow boundary"

$$\Gamma_- = \big\{(\mathbf{x},\mathbf{n}) \in \Gamma \big| \mathbf{n}_\Gamma \cdot \mathbf{n} < 0\big\}, \tag{5}$$

where $\mathbf{n}_\Gamma$ is the normal unit vector to the boundary surface Γ. The sign of the product $\mathbf{n}_\Gamma \cdot \mathbf{n}$ describes the "flow direction" of the photons across the boundary. If there are no light sources outside the modeled domain, the function g will be zero everywhere.

The left hand side of Eq. (2) will be abbreviated as an operator $\mathcal{A}$ applied to the intensity function I, yielding the very compact operator form of the radiative transfer equation

$$\mathcal{A}I(\mathbf{x},\mathbf{n}) = f(\mathbf{x}). \tag{6}$$

As already mentioned in the introduction the resulting linear system of algebraic equations is usually too large and this amount of data cannot be handled even on most advanced supercomputers. The application of efficient error estimation and grid adaption techniques is necessary to obtain reliable quantitative results. Finite element methods, in particular so-called Galerkin methods, are most suitable for these techniques (for details see [BR01] and the articles [BBR05, BKM05, BR05a, BR05b, CHR05] in this volume).

4.2 Finite Element Discretization

Equation (2) is analyzed in [DL00] and the natural space for finding solutions is

$$W = \big\{ I \in L^2(\Omega \times S^2) \;\big|\; \mathbf{n} \cdot \nabla_x I \in L^2(\Omega \times S^2)\big\}, \tag{7}$$

where L^2 is the Lebesgue space of the square integrable functions. If we consider homogeneous vacuum boundary condition, i.e. $g(\mathbf{x},\mathbf{n}) = 0$, the solution space is

$$W_0 = \big\{ I \in W \;\big|\; I = 0 \text{ on } \Gamma_-\big\}. \tag{8}$$

In order to apply a finite element method, we have to use a weak formulation of Eq. (2). Therefore, we multiply both sides of Eq. (2) by a trial function $\varphi(\mathbf{x},\mathbf{n})$ and integrate over the whole domain $\Omega \times S^2$. Thus, the weak formulation reads: Find $I \in W_0$, such that

$$\begin{aligned}
&\int_\Omega \int_{S^2} \mathbf{n} \cdot \nabla_x I(\mathbf{x},\mathbf{n}) \varphi(\mathbf{x},\mathbf{n})\, d\omega\, d^3x \\
&\quad + \int_\Omega \int_{S^2} (\kappa(\mathbf{x}) + \sigma(\mathbf{x})) I(\mathbf{x},\mathbf{n}) \varphi(\mathbf{x},\mathbf{n})\, d\omega\, d^3x \\
&\qquad - \int_\Omega \int_{S^2} \int_{S^2} \sigma(\mathbf{x}) P(\mathbf{n}',\mathbf{n}) I(\mathbf{x},\mathbf{n}') \varphi(\mathbf{x},\mathbf{n})\, d\omega'\, d\,\omega\, d^3x \\
&\qquad\quad = \int_\Omega \int_{S^2} f(\mathbf{x}) \varphi(\mathbf{x},\mathbf{n})\, d\omega\, d^3x \qquad\qquad \forall\, \varphi \in W_0.
\end{aligned} \tag{9}$$

By extending the definition of the L^2-scalar product we introduce the abbreviation

$$(I, \varphi) = (I, \varphi)_{\Omega \times S^2} = \int_{\Omega} \int_{S^2} I\varphi \, d\omega \, d^3x. \tag{10}$$

Thus, the weak formulation of the operator form in Eq. (6) is

$$(\mathcal{A}I, \varphi) = (f, \varphi) \qquad \forall\, \varphi \in W_0. \tag{11}$$

If there is no scattering, i.e. $\sigma(\mathbf{x}) = 0$ on Ω, the problem decouples to a system of stationary advection equations on Ω. These equations are hyperbolic. If the solutions are not smooth, standard finite element techniques applied to this type of equations are known to produce spurious oscillations. We can achieve stability by applying the streamline diffusion modification (see [HB82] and [Joh87]):

$$(\mathcal{A}I, \varphi + \delta \mathbf{n} \cdot \nabla_x \varphi) = (f, \varphi + \delta\, \mathbf{n} \cdot \nabla_x \varphi) \quad \forall\, \varphi \in W_0. \tag{12}$$

The cell-wise constant parameter function δ depends on the local mesh width and the coefficients κ and σ. Note that the solution of Eq. (11) also solves Eq. (12). No additional consistency error is induced since the stabilization term is simply added to Eq. (11). In the following, the streamline diffusion discretization term will be omitted but implicitly assumed.

Applying standard Galerkin finite elements to solve Eq. (11), we choose a finite dimensional subspace W_h of W consisting of functions that are piecewise polynomials with respect to a subdivision or *triangulation* $\mathbb{T}_h$ of $\Omega \times S^2$. The mesh size h is the piecewise constant function defined on each triangulation cell K by the diameter of the cell. The discrete analogon of Eq. (11) is finding $I_h \in W_h$, such that

$$(\mathcal{A}I_h, \varphi_h) = (f, \varphi_h) \quad \forall\, \varphi_h \in W_h. \tag{13}$$

The construction of the subspace W_h needs some further consideration (see [Kan96]). The discretized domain is a tensor product of two sets of completely different length scales: While Ω represents a domain in geometric space, S^2 is the unit sphere in the Euclidean space $\mathbb{R}^3$. Therefore, we use a tensor product splitting of the five-dimensional domain $\Omega \times S^2$, such that a grid cell of the five-dimensional grid will be the tensor product of a two-dimensional cell K_ω and a three-dimensional cell K_x. Accordingly, the mesh sizes with respect to $\mathbf{x}$ and ω will be different.

On S^2 we use fixed discretization based on a refined icosahedron. Quadrature points are the cell centers projected on S^2. This projection method guarantees equally distributed quadrature points, each associated with a solid angle $d\omega$ of the same size. In comparison to other numerical quadrature methods, additional symmetry conditions are redundant and discretization artifacts at the poles are avoided. Furthermore, we use piecewise constant trial functions. That way, the seven-dimensional integration of the scattering term in the

weak formulation of Eq. (9) can be calculated very efficiently. For example, the integration of the intensity over the whole unit sphere is simply replaced by a sum divided by the number of discrete ordinates M

$$\frac{1}{4\pi}\int_{S^2} I(\mathbf{n})\,d\omega \to \frac{1}{M}\sum_{j=1}^{M} I_j\,. \tag{14}$$

Nevertheless, our scheme is second order accurate in the evaluated ordinate points due to super-convergence (see [Kan96]).

For the space domain Ω we use locally refined hexahedral meshes. The mesh size of the spatial cell K_x is denoted by h. Since the boundaries are arbitrary for our astrophysical applications, we can choose a unit cube for Ω and place the simulation object within this cube. We only have ensure that the boundary of Ω is far away from the simulation object where the photons may freely escape towards the observer. Thus, we do not have to worry about boundary approximations. We use continuous piecewise trilinear trial functions in space.

4.3 Error Estimation and Adaptivity

The calculation of complex radiation fields in astrophysics often requires high resolution in parts of the computational domain, for example in regions with strong opacity gradients. Then, reliable error bounds are necessary to rule out numerical errors. Due to the high dimension of the radiative transfer problem, a well suited method for error estimation and grid adaptation is necessary to achieve results of sufficient accuracy even with the storage capacities of parallel computers.

In addition, computational goals in astrophysics are often more specific. The result of a simulation is to be compared with observations to develop a physical model for the celestial object. For instance, in the case of a distant unresolved object, the radiative energy emanating the domain Ω in *one* particular direction, i.e. the direction towards the observer, is of interest. Generally, a measured quantity like the radiative energy can be expressed as a linear functional $\mathcal{M}(I)$. By linearity, the error of the measured quantity is $\mathcal{M}(I) - \mathcal{M}(I_h) = \mathcal{M}(e)$, where $e = I - I_h$. In the following, we will show that it is possible to obtain an *a-posteriori* estimate for $\mathcal{M}(e)$, even if the exact solution I is unknown.

Suppose, $z(\mathbf{x}, \mathbf{n})$ is the solution of the dual problem

$$\mathcal{M}(\varphi) = (\varphi, \mathcal{A}^* z) \qquad \forall\, \varphi \in W_0, \tag{15}$$

where the dual radiative transfer operator is defined by

$$\begin{aligned}\mathcal{A}^* z(\mathbf{x}, \mathbf{n}) = &-\mathbf{n}\cdot\nabla_x z(\mathbf{x}, \mathbf{n}) + \big(\kappa(\mathbf{x}) + \sigma(\mathbf{x})\big) z(\mathbf{x}, \mathbf{n}) \\ &-\sigma(\mathbf{x}) \int_{S2} P(\mathbf{n}', \mathbf{n}) z(\mathbf{x}, \mathbf{n}')\,d\omega'.\end{aligned} \tag{16}$$

The boundary conditions for the dual problem are complementary to those in the primal problem, i.e. $I = 0$ on the "outflow boundary" $\Gamma_+ = \{(\mathbf{x}, \mathbf{n}) \in \Gamma \mid \mathbf{n}_\Gamma \cdot \mathbf{n} > 0\}$. Then, we get the formal error representation

$$\begin{aligned} \mathcal{M}(e) = (e, \mathcal{A}^* z) &= (\mathcal{A}e, z) \\ &= (\mathcal{A}e, z - z_i) \\ &= \sum_{K \in \mathbb{T}_h} \left(f - \mathcal{A}I_h, z - z_i\right)_K \end{aligned} \tag{17}$$

for arbitrary $z_i \in W_h$. In the second line of Eq. (17) a characteristic feature of finite element methods is used, the so-called Galerkin orthogonality

$$(\mathcal{A}I - \mathcal{A}I_h, \varphi_h) = 0 \qquad \forall\, \varphi_h \in W_h. \tag{18}$$

Since the dual solution z is unknown, it is a usual approach to apply Hölder's inequality and standard approximation estimates of finite element spaces [4] to obtain the duality-based a-posteriori error estimate ("DRW method"; see [BR01] and the articles [BBR05, BKM05, BR05a, BR05b, CHR05] in this volume)

$$\mathcal{M}(e) \le \eta = \sum_{K \in \mathbb{T}_h} \eta_K \ , \qquad \eta_K = C_K h_K^2 \|\varrho\|_K \|\nabla^2 z\|_K, \tag{19}$$

where the constant C_K is determined by local approximation properties of W_h. The residual function ϱ of I_h is defined by $\varrho = f - \mathcal{A}I_h$. Since the dual solution z is not available analytically, it is usually replaced by the finite element solution z_h to the dual problem in Eq. (15). This involves a second solution step of the same structure as the primal problem. It is clear, that by this replacement the error estimate in Eq. (19) is not strictly true anymore. Experience shows that the additional error is small and the estimate may be used if multiplied with a modest security factor larger than one (for details see [BR01]).

A first approach in the development of strategies for grid refinement based on a-posteriori error estimates is the control of the global energy or L^2-error involving only local residuals of the computed solution (see [FK97]). Formally, using the functional $\mathcal{M}(\varphi) = \|e\|^{-1}(e, \varphi)$ in Eq. (15), we obtain $\mathcal{M}(e) = \|e\|^{-1}(e, e) = \|e\|$ for the left hand side of (17). An estimate of the right hand side of Eq. (17) yields

$$\|e\| \le \tilde{\eta} = \sqrt{\sum_{K \in \mathbb{T}_h} \eta_{L^2}^2} \ , \qquad \eta_{L^2} = C_K C_s h_K^2 \|\varrho\|_K. \tag{20}$$

In this estimate, the information about the global error sensitivities contained in the dual solution is condensed into just one "stability constant"

[4] for details see [BR01] and the standard Bramble-Hilbert theory in [BH71]

$C_s = \left\|\nabla^2 z\right\|$. This is appropriate in estimating the global L^2-error in case of constant coefficients. For more general situations with strongly varying coefficients, it may be advisable rather to follow the "DRW approach" in which the information from the dual solution is kept within the a-posteriori error estimator defined in Eq. (19). Nevertheless, the L^2-indicator η_{L^2} in Eq. (20) provides a reasonable grid refinement criterion to study the qualitative behavior of the solution I everywhere in Ω (see [WMK99] for an illustration of this approach).

The grid refinement process on the basis of an a-posteriori error estimate is organized in the following way: Suppose that some error tolerance TOL is given. The aim is to find the most economical grid $\mathbb{T}_h$ on which

$$|\mathcal{M}(e)| \leq \hat{\eta}(I_h) = \sqrt{\sum_{K \in \mathbb{T}_h} \eta_K^2(I_h)} \leq TOL, \tag{21}$$

with *local refinement indicators* η_K taken from Eq. (19). A qualitative investigation of grids obtained via different adaptive refinement criteria, e.g. Eq. (19) and Eq. (20), is published in [RM01]. Having computed the solution on a coarse grid, the so-called *fixed fraction* grid refinement strategy (see [Kan96], [BR01]) is applied: The cells are ordered according to the size of η_K and a fixed portion ν (say 30%) of the cells with largest η_K is refined. This guarantees, that in each refinement cycle a sufficient large number of cells is refined. Then, a solution is computed on the new grid and the process is continued until the prescribed tolerance is achieved. This algorithm is especially valuable, if a computation "as accurate as possible" is desired, that is, the tolerance is not reached, but computer memory is exhausted. Then, the parameter ν has to be determined by the remaining memory resources.

4.4 Resulting Matrix Structure

Given a discretization with N vertices in Ω and M ordinates in S^2, the discrete system has the form

$$\mathbf{A} \cdot \mathbf{u} = \mathbf{f}, \tag{22}$$

with the vector $\mathbf{u}$ containing the discrete specific intensities and the vector $\mathbf{f}$ the values of the source term. Both vectors are of length $(N \cdot M)$. $\mathbf{A}$ is a $(N \cdot M) \times (N \cdot M)$ matrix. Applying the tensor product structure proposed above, we may write

$$\mathbf{A} = \mathbf{T} + \mathbf{K} + \mathbf{S} \tag{23}$$

with the block structure

$$\mathbf{T} = \begin{pmatrix} \mathbf{T}_1 & & \mathbf{0} \\ & \ddots & \\ \mathbf{0} & & \mathbf{T}_M \end{pmatrix}, \qquad \mathbf{K} = \begin{pmatrix} \mathbf{K}_1 & & \mathbf{0} \\ & \ddots & \\ \mathbf{0} & & \mathbf{K}_M \end{pmatrix},$$

$$\mathbf{S} = \begin{pmatrix} \omega_{11}\mathbf{S}_1 & \dots & \omega_{1M}\mathbf{S}_1 \\ \vdots & \ddots & \vdots \\ \omega_{M1}\mathbf{S}_M & \dots & \omega_{MM}\mathbf{S}_M \end{pmatrix},$$

where $\omega_{il} = P(\mathbf{n}_i, \mathbf{n}_l)/M$. If we account for the finite element streamline diffusion discretization as described in Eq. (12), the entries of the $N \times N$ blocks are defined by

$$\begin{aligned} \mathbf{T}_i^{jk} &= (\varphi_j + \delta\mathbf{n}_i \cdot \nabla_x\varphi_j, \mathbf{n}_i \cdot \nabla_x\varphi_k) \\ \mathbf{K}_i^{jk} &= (\varphi_j + \delta\mathbf{n}_i \cdot \nabla_x\varphi_j, (\kappa + \sigma)\,\varphi_k) \\ \mathbf{S}_i^{jk} &= (\varphi_j + \delta\mathbf{n}_i \cdot \nabla_x\varphi_j, \sigma\varphi_k)\,, \end{aligned}$$

where $j = 1, ..., N$ and $k = 1, ..., N$.

4.5 Iterative Methods

The linear system of equations resulting from the discretization described above is large (10^7 unknowns at least), sparse, and strongly coupled due to the integral operator. Usually, an iterative scheme is applied to solve such large systems of equations (e.g., see [Hac93, Var00]). The standard algorithm used in astrophysics in this case is the so-called Λ- or Source Iteration method [Mih78] which can be viewed as a form of the Richardson method with nearly block-Jacobi-preconditioning. Use of a full Jacobi preconditioner is a first step towards better convergence rates [Tur93]. Since the transport operator is inverted explicitly, these methods converge very fast for transport dominated problems. If, further, the triangular matrix structure of upwind-discretizations is exploited, the inversion is indeed very cheap (one matrix-vector-multiplication).

Unfortunately, the present interest is in opaque and highly scattering media where this method – like other stationary iterations – breaks down, because the condition number of the iteration matrix becomes very large. Since the convergence rate of preconditioned Richardson iteration methods exclusively depends on the condition number, stationary iterations are not suited for the scattering dominated case. It can be shown, though, that the eigenvalue distribution of the transport matrix is clustered, with one eigenvalue located at the origin, while the others are close to unity or at least bounded away from zero (for details see [Kan96]). Krylov space methods like GMRES or bi-CGSTAB described in [SF93] are particular suited to deal with such a type of eigenvalue distribution. While Krylov-type solvers are superior to stationary iteration methods, they still have poor convergence properties for scattering-dominated

and opaque transfer problems, so that convergence acceleration methods need to be brought in. During the last several decades, significant progress has been achieved in the development of acceleration methods, i.e. preconditioning methods, which were designed to speed up the iterative convergence of discrete-ordinates approaches. A comprehensive review recently appeared in the literature (see [AL02]), covering the main methods that have been proposed. Of all the acceleration methods, the Diffusion Synthetic Acceleration (DSA) is one of the most efficient preconditioning methods, guaranteeing rapid convergence for all optical thicknesses and scattering values. In Sect. 8 a DSA-type preconditioner is presented that acts like a smoothing operator for specific intensities and which corresponds to a multilevel method for the diffusion approximation of the mean intensity. The word "multilevel" or "multigrid" often connotes a sequence of increasingly coarse spatial meshes. However, for transport problems, space and angle are variables, and the method we consider involves "collapsing" the transport problem onto "coarser grids" independent of the photon direction. It is demonstrated that the method allows to arrive at a fast solution of discrete linear problems in those cases where scattering is dominant as well as when transition regions occur.

4.6 Parallelization

Transport dominated problems differ in one specific point from elliptic problems: There is a distinct direction of information flow. This has to be considered in the development of parallelization strategies. While a domain decomposition for Poisson's equation should minimize the length of interior edges, this does not yield an efficient method for transport equations.

In [Kan00], it was concluded that parallelization strategies for transport equations should not divide the domain across the transport direction. The solution of the radiative transfer equation consists of a number of transport inversions for different photon propagation directions. The construction of an efficient domain decomposition method would require a direction dependent splitting of the domain Ω. Since this causes immense implementation problems, we decided to use ordinate parallelization.

This strategy distributes the ordinate space S^2 of the radiative transfer equation. Since we use discontinuous shape functions for the ordinate variable and there is no local coupling due to the integral operator, this results in a true non-overlapping parallelization. Clearly, it has disadvantages, too. As the scattering integral is a global operator, ordinate parallelization involves global communication. In add, the resolution in space is restricted by the per node memory and not by the total memory of the machine. In [RM01] memory and CPU time requirements are investigated for a test model configuration distributing the ordinate space S^2 over 1 to 16 processors. The results show that the code scales optimal (i.e. double the number of processors, halves the required CPU time and memory) for parallel applications.

5 Polychromatic 3D Line Transfer

In the following an algorithm modeling polychromatic, i.e. frequency-dependent, 3D radiation fields in moving media is presented. This extension of the monochromatic model described in the previous section is required, since the radiation field is of major importance for the energy transfer in many differentially moving celestial objects like novae, supernovae, collapsing molecular clouds, collapsing and expanding or rotating gas clouds (halos), and accretion discs. Additionally, resonance line profiles are strongly affected by radiative transfer processes, providing deep insight into the density structure and the nature of the macroscopic velocity field of the emanating object.

The present work aims at the modeling of 3D radiation fields in gas clouds from the early universe, in particular as to the influence of varying distributions of density and velocity. In observations of high-redshift gas clouds (halos), the Lyα transition from the first excited energy level to the ground state of the hydrogen atom is usually found to be the only prominent emission line in the entire spectrum. It is a well-known assumption that high-redshifted hydrogen clouds are the precursors of present-day galaxies. Thus, the investigation of the Lyα line is of paramount importance for the theory of galaxy formation and evolution. The observed Lyα line – or rather, to be precise, its profile – reveals both the complexity of the spatial distribution and of the kinematics of the interstellar gas, and also the nature of the photon source.

The transfer of resonance line photons is profoundly determined by scattering in space and frequency. Analytical (see [Neu90]) as well as early numerical methods [Ada72, HK80] were restricted to one-dimensional, static media. Only recently, codes based on the Monte Carlo method were developed which are capable to investigate the more general case of a multi-dimensional medium (see [ALL01, ALL02, ZM02]).

5.1 Line Transfer in Moving Media

The frequency-dependent radiation field in moving media is obtained by solving the non-relativistic radiative transfer equation in a co-moving frame (for details see [WBW00]). For a three-dimensional domain Ω the operator form of the equation is

$$\big(\mathcal{T} + \mathcal{D} + \mathcal{S} + \chi(\mathbf{x}, \nu)\big)\mathcal{I}(\mathbf{x}, \mathbf{n}, \nu) = f(\mathbf{x}, \nu). \tag{24}$$

$\mathcal{T}$ is the transfer operator, $\mathcal{D}$ the "Doppler" operator, and $\mathcal{S}$ the scattering operator, which are defined as follows

$$\begin{aligned}
\mathcal{T}\mathcal{I}(\mathbf{x}, \mathbf{n}, \nu) &= \mathbf{n} \cdot \nabla_x \mathcal{I}(\mathbf{x}, \mathbf{n}, \nu), \\
\mathcal{D}\mathcal{I}(\mathbf{x}, \mathbf{n}, \nu) &= w(\mathbf{x}, \mathbf{n})\, \nu \frac{\partial}{\partial \nu} \mathcal{I}(\mathbf{x}, \mathbf{n}, \nu), \\
\mathcal{S}\mathcal{I}(\mathbf{x}, \mathbf{n}, \nu) &= -\frac{\sigma(\mathbf{x})}{4\pi} \int_0^\infty \int_{S^2} R(\hat{\mathbf{n}}, \hat{\nu}; \mathbf{n}, \nu) \mathcal{I}(\mathbf{x}, \hat{\mathbf{n}}, \hat{\nu})\, d\hat{\omega}\, d\hat{\nu}.
\end{aligned}$$

The relativistic invariant specific intensity $\mathcal{I}$ is a function of six variables, three of which give the spatial location $\mathbf{x}$, while two variables give the direction $\mathbf{n}$ (pointing in the direction of the solid angle $d\omega$ of the unit sphere S^2), and one variable gives the frequency ν.

The extinction coefficient $\chi(\mathbf{x},\nu) = \kappa(\mathbf{x},\nu) + \sigma(\mathbf{x},\nu)$ is the sum of the absorption coefficient $\kappa(\mathbf{x},\nu) = \kappa(\mathbf{x})\varphi(\nu)$ and the scattering coefficient $\sigma(\mathbf{x},\nu) = \sigma(\mathbf{x})\varphi(\nu)$. The frequency-dependence is given by a normalized profile function $\varphi \in L^1(R^+)$. The core of the Lyα line is dominated by Doppler broadening. The effects of radiation and resonance damping may be important in the wings of the line at low column densities. Under the assumption that these mechanisms are all uncorrelated, one can account for their combined effects by a convolution procedure. The folding of the Doppler profile with the Lorentz profiles from radiation and resonance damping gives a Voigt profile, which is the general description of Lyα line profiles (see [Mih78]). For all applications presented in this paper $v_{\text{turb}} \gg v_{\text{therm}}$ is adopted. This results in a very broad Doppler core dominating the Lorentzian wings of the Voigt profile. Thus, a Doppler profile

$$\varphi(\nu) = \frac{1}{\sqrt{\pi}\,\Delta\nu_D} \exp\left[-\left(\frac{\nu-\nu_0}{\Delta\nu_D}\right)^2\right] \tag{25}$$

is a reasonable description of a Lyα line profile, where ν_0 is the frequency of the line center and c is the speed of light. The Doppler width $\Delta\nu_D$ and the Doppler velocity v_D are determined by a thermal velocity v_{therm} and a small scale turbulent velocity v_{turb},

$$\Delta\nu_D = \frac{\nu_0}{c} v_D = \frac{\nu_0}{c}\sqrt{v_{\text{therm}}^2 + v_{\text{turb}}^2}. \tag{26}$$

For the source term

$$f(\mathbf{x},\nu) = \kappa(\mathbf{x},\nu)B(T(\mathbf{x}),\nu) + \epsilon(\mathbf{x},\nu), \tag{27}$$

we can consider thermal radiation and non-thermal radiation. In the case of thermal radiation, f is calculated from a temperature distribution $T(\mathbf{x})$, where $B(T,\nu)$ is the Planck function.

The "Doppler" operator $\mathcal{D}$ causes the Doppler shift of the photons. A derivation for non-relativistic moving media [5] can be found in [WBW00]. The basis of the derivation is a "simplified" Lorentz transformation, which, in fact, is a Galilei transformation in combination with a linear Doppler formula. We restrict ourselves to sufficiently small velocity fields, and furthermore neglect aberration and advection effects, i.e. the photon propagation direction $\mathbf{n}$ is kept unchanged during the transformation. The function

$$w(\mathbf{x},\mathbf{n}) = -\mathbf{n}\cdot\nabla_x\left(\mathbf{n}\cdot\frac{\mathbf{v}(\mathbf{x})}{c}\right) \tag{28}$$

[5] This includes velocities fields up to approximately 10% of the speed of light

is the gradient of the velocity field $\mathbf{v}(\mathbf{x})$ in direction $\mathbf{n}$. Note that the sign of w may change depending on the complexity of the velocity field $\mathbf{v}$.

Line transfer problems often include scattering processes where both the direction and the frequency of a photon may be changed. These changes are described by a general redistribution function $R(\hat{\mathbf{n}}, \hat{\nu}; \mathbf{n}, \nu)$ which gives the joint probability that a photon will be scattered from direction $\hat{\mathbf{n}}$ in solid angle $d\hat{\omega}$ and frequency range $(\hat{\nu}, \hat{\nu} + d\hat{\nu})$ into solid angle $d\omega$ in direction $\mathbf{n}$ and frequency range $(\nu, \nu + d\nu)$. If we assume that the radiation field is nearly isotropic, the scattering process may be approximated by

$$\mathcal{S}\mathcal{I} = -\frac{\sigma(\mathbf{x})}{4\pi} \int_0^\infty R(\hat{\nu}, \nu) \int_{S^2} \mathcal{I}(\mathbf{x}, \hat{\mathbf{n}}, \hat{\nu})\, d\hat{\omega}\, d\hat{\nu}, \tag{29}$$

where $R(\hat{\nu}, \nu)$ is the angle-averaged redistribution function

$$R(\hat{\nu}, \nu) = \frac{1}{(4\pi)^2} \int_{S^2} \int_{S^2} R(\mathbf{x}, \hat{\mathbf{n}}, \hat{\nu}; \mathbf{n}, \nu)\, d\hat{\omega}\, d\omega. \tag{30}$$

The function defined by Eq. (30) is normalized such that

$$\int_0^\infty \int_0^\infty R(\hat{\nu}, \nu)\, d\hat{\nu}\, d\nu = 1. \tag{31}$$

For the calculations in Sect. 5.3, we consider two limiting cases: strict coherence and complete redistribution in the comoving frame. In the former case, we have

$$R(\hat{\nu}, \nu) = \varphi(\hat{\nu})\delta(\nu - \hat{\nu}), \tag{32}$$

and in the latter

$$R(\hat{\nu}, \nu) = \varphi(\hat{\nu})\varphi(\nu). \tag{33}$$

Thus, for coherent isotropic scattering, the scattering term simplifies to

$$\mathcal{S}^{\mathrm{coh}}\mathcal{I}(\mathbf{x}, \mathbf{n}, \nu) = -\frac{\sigma(\mathbf{x}, \nu)}{4\pi} \int_{S^2} \mathcal{I}(\mathbf{x}, \hat{\mathbf{n}}, \nu)\, d\hat{\omega} \tag{34}$$

In the case of complete redistribution, the photons are scattered isotropically in angle, but are randomly redistributed over the line profile. Then, the scattering term reads

$$\mathcal{S}^{\mathrm{crd}}\mathcal{I}(\mathbf{x}, \mathbf{n}, \nu) = -\frac{\sigma(\mathbf{x}, \nu)}{4\pi} \int_0^\infty \varphi(\hat{\nu}) \int_{S^2} \mathcal{I}(\mathbf{x}, \hat{\mathbf{n}}, \hat{\nu})\, d\hat{\omega}\, d\hat{\nu}. \tag{35}$$

5.2 Boundary Conditions

Formally, the frequency derivative in the Doppler term of (24) can be viewed as being similar to the time derivative for non-stationary radiative transfer or

heat transfer problems, so that a parabolic system of initial value problems is obtained. Unfortunately, the Doppler term also contains a function $w(\mathbf{x}, \mathbf{n})$, which is essentially the gradient of the macroscopic velocity field, multiplied by the photon propagation direction $\mathbf{n}$ (cf. (28)). Depending on the complexity of the velocity field, this function $w(\mathbf{x}, \mathbf{n})$ may change its sign at different points $\mathbf{x}$ and for different directions $\mathbf{n}$ when setting up the initial value either on the lower or upper frequency boundary. In this paper we take this into account by defining an additional frequency boundary value problem, which involves a "frequency inflow boundary" $\Sigma^- = \Omega \times S^2 \times \partial\Lambda$ depending on the sign of $w(\mathbf{x}, \mathbf{n})$. In order to solve (24) correctly, boundary conditions of the form

$$\mathcal{I}(\mathbf{x}, \mathbf{n}, \nu) = p(\mathbf{x}, \mathbf{n}, \nu) \qquad \text{on } \Gamma^- \times \Lambda \qquad \text{and} \tag{36}$$

$$\mathcal{I}(\mathbf{x}, \mathbf{n}, \nu) = q(\mathbf{x}, \mathbf{n}, \nu) \qquad \text{on } \Sigma^-. \tag{37}$$

must be imposed. The "spatial inflow boundary" is

$$\Gamma^- \times \Lambda = \Big\{(\mathbf{x}, \mathbf{n}, \nu) \in \Gamma \;\Big|\; \mathbf{n}_\Gamma \cdot \mathbf{n} < 0\Big\}, \tag{38}$$

where $\mathbf{n}_\Gamma$ is the normal unit vector to the boundary surface Γ of the spatial domain Ω. The sign of the product $\mathbf{n}_\Gamma \cdot \mathbf{n}$ describes the "flow direction" of the photons across the boundary of the spatial domain. For our modeling of the spectral Lyα line, we assume that there is no continuum emission "outside of the line" and that there are no light sources "outside the modeled domain". In this case the two boundary conditions for the solution of the transfer equation (24) in moving media are

$$\mathcal{I}(\mathbf{x}, \mathbf{n}, \nu) = 0 \qquad \text{on } \Sigma^-, \tag{39}$$

$$\mathcal{I}(\mathbf{x}, \mathbf{n}, \nu) = 0 \qquad \text{on } \Gamma^- \times \Lambda. \tag{40}$$

5.3 Finite Element Discretization

The simultaneous Galerkin discretization in space-frequency is, from a theoretical point of view, an extremely appealing approach. Considering the memory requirement, the solution of the complete algebraic system resulting from this discretization is by far too "expensive". With a view to reducing the memory demand, a discretization first in space and then in frequency is performed. This approach is called method of lines and finally results in a system of ordinary differential equations. Contrary to the continuous Galerkin discretization in space, the discretization in frequency is a discontinuous Galerkin (DG) method. It is important to note that the above discretization in space and in frequency can be interpreted as a simultaneous Galerkin discretization in the space-frequency domain. The frequency DG method is performed by using piecewise polynomials of degree zero, which corresponds to an implicit Euler method for N equidistantly distributed frequency points $\nu_i \in \{\nu_1, \nu_2, ..., \nu_N\} \subset \Lambda$ (see [Boe96]). DG methods are not only used for

discretizing ordinary differential equations, especially initial value problems, but also for the time discretization and mesh control of partial differential equations as described in [EJ87, EJ91] and [EJT85].

Discretization for Coherent Scattering

In order to solve the radiative transfer equation (24), we first carry out the frequency discretization including coherent scattering. With the abbreviation

$$\mathcal{A}^{\mathrm{coh}} = \mathcal{T} + \mathcal{S}^{\mathrm{coh}} + \chi(\mathbf{x}, \nu) \tag{41}$$

Eq. (24) can be written as

$$\mathcal{A}^{\mathrm{coh}}\mathcal{I}(\mathbf{x}, \mathbf{n}, \nu) + w(\mathbf{x}, \mathbf{n})\nu \frac{\partial}{\partial \nu}\mathcal{I}(\mathbf{x}, \mathbf{n}, \nu) = f(\mathbf{x}, \nu). \tag{42}$$

Since the function $w(\mathbf{x}, \mathbf{n})$ may change its sign, this simple difference scheme for the Doppler term reads

$$w(\mathbf{x}, \mathbf{n})\nu \frac{\partial \mathcal{I}}{\partial \nu} \longrightarrow w\nu_i \frac{\mathcal{I}_i - \mathcal{I}_{i-1}}{\Delta\nu} \qquad (w_i > 0), \tag{43}$$

and

$$w(\mathbf{x}, \mathbf{n})\nu \frac{\partial \mathcal{I}}{\partial \nu} \longrightarrow w\nu_i \frac{\mathcal{I}_{i+1} - \mathcal{I}_i}{\Delta\nu} \qquad (w_i < 0), \tag{44}$$

where $\Delta\nu$ is the constant frequency step size. All quantities referring to the discrete frequency point ν_i are denoted by an index "i". Employing the Euler method, we get a semi-discrete representation of Eq. (42)

$$\Big(\mathcal{A}_i^{\mathrm{coh}} + \frac{|w|\nu_i}{\Delta\nu}\Big)\mathcal{I}_i = f_i + \frac{|w|\nu_i}{\Delta\nu} \begin{cases} \mathcal{I}_{i-1} & (w > 0) \\ \mathcal{I}_{i+1} & (w < 0) \end{cases}. \tag{45}$$

The additional term on the left side of Eq. (45) can be interpreted as an artificial opacity, which is advantageous for the solution of the resulting linear system of equations. The additional term on the right side of Eq. (45) is included as an artificial source term. Equation (45) can be written in a compact operator form

$$\tilde{\mathcal{A}}_i^{\mathrm{coh}}\mathcal{I}_i = \tilde{f}_i. \tag{46}$$

Given a discretization with L degrees of freedom in Ω, M directions on the unit sphere S^2 and N frequency points, the overall discrete system has the matrix form

$$\mathbf{A}^{\mathrm{coh}}\mathbf{u} = \mathbf{f}, \tag{47}$$

with the vector $\mathbf{u}$ containing the discrete intensities and the vector $\mathbf{f}$ the values of the source term for all frequency points ν_i. Both vectors are of length $(L \cdot M \cdot N)$ and $\mathbf{A}^{\mathrm{coh}}$ is a $(L \cdot M \cdot N) \times (L \cdot M \cdot N)$ matrix. The fact

that the function $w(\mathbf{x},\mathbf{n})$ may change its sign, results in a block-tridiagonal structure of $\mathbf{A}^{\mathrm{coh}}$ and we get

$$\begin{pmatrix} \tilde{\mathbf{A}}_1^{\mathrm{coh}} & \mathbf{R}_1 & \mathbf{0} & \dots & \mathbf{0} \\ \mathbf{B}_2 & \tilde{\mathbf{A}}_2^{\mathrm{coh}} & \mathbf{R}_2 & \ddots & \vdots \\ \mathbf{0} & \ddots & \ddots & \ddots & \mathbf{0} \\ \vdots & \ddots & \ddots & \ddots & \mathbf{R}_{N-1} \\ \mathbf{0} & \dots & \mathbf{0} & \mathbf{B}_N & \tilde{\mathbf{A}}_N^{\mathrm{coh}} \end{pmatrix} \begin{pmatrix} \mathbf{u}_1 \\ \mathbf{u}_2 \\ \vdots \\ \vdots \\ \mathbf{u}_N \end{pmatrix} = \begin{pmatrix} \mathbf{f}_1 \\ \mathbf{f}_2 \\ \vdots \\ \vdots \\ \mathbf{f}_N \end{pmatrix}. \tag{48}$$

According to the sign of $w(\mathbf{x},\mathbf{n})$ the block matrices $\mathbf{R}_i$ and $\mathbf{B}_i$ hold entries of $w(\mathbf{x},\mathbf{n})\nu_i/\Delta\nu$ causing a redshift and blueshift of the photons in the medium, respectively. Requiring a reasonable resolution, the resulting linear system of equations of the total system is too large to be solved directly. Hence, we are treating N "monochromatic" radiative transfer problems

$$\tilde{\mathbf{A}}_i^{\mathrm{coh}}\mathbf{u}_i = \tilde{\mathbf{f}}_i, \tag{49}$$

with a slightly modified right hand side

$$\tilde{\mathbf{f}}_i = \mathbf{f}_i + \mathbf{R}_i\mathbf{u}_{i+1} + \mathbf{B}_i\mathbf{u}_{i-1}. \tag{50}$$

Note that using simple velocity fields (e.g. collapse or expansion of a gas cloud) the sign of $w(\mathbf{x},\mathbf{n})$ is fixed and the matrix $\mathbf{A}^{\mathrm{coh}}$ has a block-bidiagonal structure. This is favorable for our solution strategy, since we only need to solve Eq. (49) once for each frequency point.

Discretization for Complete Redistribution

In order to include complete redistribution, we use a simple quadrature method for the frequency integral in the scattering operator $\mathcal{S}^{\mathrm{crd}}$ in Eq. (35). The Doppler term is discretized using an implicit Euler scheme as described in the previous section. Starting from N equidistantly distributed frequency points $\nu_i \in \{\nu_1,\nu_2,...,\nu_N\} \subset \Lambda$ and N weights $q_1,q_2,...,q_N$, we define a quadrature method

$$Q(\nu_i) := \sum_{j=1}^{N} q_j\xi(\nu_j) \tag{51}$$

for integrals $\int_\Lambda \xi(\nu')d\nu'$. In the case of complete redistribution the kernel is

$$\xi(\nu_j) = \frac{\varphi(\nu_j)}{4\pi}\int_{S^2}\mathcal{I}(\mathbf{x},\hat{\mathbf{n}},\nu_j)d\hat{\omega}, \tag{52}$$

and the semi-discretized scattering integral in Eq. (35) for a particular frequency point $\ni_i$ reads

$$\frac{\sigma_i}{4\pi}\varphi_i q_i \int_{S^2} \mathcal{I}_i d\hat{\omega} + \frac{\sigma_i}{4\pi}\sum_{j\neq i}^{N} \varphi_j q_j \int_{S^2} \mathcal{I}(\mathbf{x},\hat{\mathbf{n}},\nu_j) d\hat{\omega}. \tag{53}$$

With this scattering operator the semi-discrete formulation of the transfer problem for each frequency point $\ni_i$ is

$$\Big(\mathcal{A}_i^{\mathrm{crd}} + \frac{|w|\nu_i}{\Delta\nu}\Big)\mathcal{I}_i = \tilde{f}_i + \frac{\sigma_i}{4\pi}\sum_{j\neq i}^{N} \varphi_j q_j \int_{S^2} \mathcal{I}(\mathbf{x},\hat{\mathbf{n}},\nu_j) d\hat{\omega}, \tag{54}$$

where

$$\mathcal{A}_i^{\mathrm{crd}} = \mathcal{T} + \chi_i + \varphi_i q_i \mathcal{S}^{\mathrm{coh}}. \tag{55}$$

The additional terms on the right hand side of Eq. (54) must be interpreted as artificial source terms. Eq. (54) can also be written in a compact operator form

$$\tilde{\mathcal{A}}_i^{\mathrm{crd}} \mathcal{I}_i = \hat{f}_i. \tag{56}$$

The total discrete system has the matrix form (cf. Eq. (47))

$$\mathbf{A}^{\mathrm{crd}}\mathbf{u} = \mathbf{f}. \tag{57}$$

Unfortunately, the global frequency coupling via the scattering integral in Eq. (35) results in a full block matrix and we get

$$\mathbf{A}^{\mathrm{crd}} = \begin{pmatrix} \tilde{\mathbf{A}}_1^{\mathrm{crd}} & \mathbf{R}_1 + \mathbf{Q}_2 & \mathbf{Q}_3 & \dots & \mathbf{Q}_N \\ \mathbf{B}_2 + \mathbf{Q}_1 & \tilde{\mathbf{A}}_2^{\mathrm{crd}} & \mathbf{R}_2 + \mathbf{Q}_3 & \ddots & \vdots \\ \mathbf{Q}_1 & \ddots & \ddots & \ddots & \vdots \\ \vdots & \ddots & \ddots & \ddots & \vdots \\ \mathbf{Q}_1 & \dots & \dots & \dots & \tilde{\mathbf{A}}_N^{\mathrm{crd}} \end{pmatrix}. \tag{58}$$

$\mathbf{B}_i$ and $\mathbf{R}_i$ again contain the contribution of the Doppler factor $w(\mathbf{x},\mathbf{n})\nu_i/\Delta\nu$, whereas $\mathbf{Q}_j$ holds the terms from the quadrature scheme. As we already explained in the case of coherent scattering, we do not directly solve the total system, but successively solve N "monochromatic" radiative transfer problems

$$\tilde{\mathbf{A}}_i^{\mathrm{crd}} \mathbf{u}_i = \hat{\mathbf{f}}_i, \tag{59}$$

successively, with a modified right hand side

$$\hat{\mathbf{f}}_i = \mathbf{f}_i + \mathbf{R}_i \mathbf{u}_{i+1} + \mathbf{B}_i \mathbf{u}_{i-1} + \sum_{j\neq i} \mathbf{Q}_j \mathbf{u}_j. \tag{60}$$

5.4 Full Solution Algorithm

Equation (46) and (56) are of the same form as the monochromatic radiative transfer equation, cf. Eq. (6), for which we propose a solution method based on a finite element technique in Sect. 4. The finite element method employs hierarchically structured grids which are locally refined by means of duality-based a-posteriori error estimates. Now, we apply this method to Eq. (46) or Eq. (56). The solution is obtained using an iterative procedure, where quasi-monochromatic radiative transfer problems are solved successively. In brief, the full solution algorithm reads:

1. Start with $\mathcal{I} = 0$ for all frequencies.
2. Solve Eq. (47) or Eq. (57) for $i = 1, .., N$.
3. Repeat step 2 until convergence is reached.
4. Refine grid and repeat steps 2 and 3.

We start with a relatively coarse grid, where only the most important structures are pre-refined, and assure that the frequency interval $[\nu_1, \nu_N]$ is wide enough to cover the total line profile. Then, we solve Eq. (46) or Eq. (56) for each frequency several times depending on the choice of the redistribution function and the velocity field. During this fixed point iteration, we monitor the changes of the resulting line profile in a particular direction $\mathbf{n}_{\text{out}}$. When the line profile remains unchanged, we turn to step 4 and refine the spatial grid. Again, we apply the fixed fraction grid refinement strategy: The cells are ordered according to the size of the local refinement indicator $\eta_K = \max(\eta_K(\nu_i))|_{\nu_i}$ and a fixed portion of the cells with largest η_K is refined. $\eta_K(\nu_i)$ is an indicator for the error contribution of the solution in cell K at frequency ν_i.

6 Test Calculations

The simple 3D test calculations presented in this section use a spherically symmetric density distribution of the form

$$\chi(\mathbf{x}) = \begin{cases} \chi_0/(1+\alpha r_c^2) & \text{for } r \le r_c, \\ \chi_0/(1+\alpha r^2) & \text{for } r_c < r \le r_h, \\ \chi_0/(1+\alpha r_h^2)/10^3 & \text{for } r > r_h, \end{cases} \tag{61}$$

where r_c is a constant core radius in the center of the halo. The halo radius is r_h and the square of the radius is $r^2 = x^2 + y^2 + z^2$. The constant opacity χ_0 is determined by the line center optical depth

$$\tau = \int_{r_c}^{r_h} \chi(\mathbf{x})\varphi(\nu_0)\ \mathbf{n}_{\text{thick}}\, d\mathbf{x} \tag{62}$$

between r_c and r_h along the most optical thick photon direction $\mathbf{n}_{\text{thick}}$. In total, the spatial distribution of χ is determined by three parameters: the

radii r_c and r_h, the dimensionless parameter α, and the optical depth τ. For r_c, r_h and α we use the values given in Table 2.

Since we are predominantly interested in the transfer of radiation in resonance lines like Lyα, we assume $\sigma(\mathbf{x}) = \chi(\mathbf{x})$ and $\kappa(\mathbf{x}) = 0$ for all calculations presented here. This restricts us to the use of a given source function. In particular, we consider a single spatially confined source region located at the origin of the unit cube at the position $\mathbf{x}_i = 0$ with radius r_s:

$$f(\mathbf{x}, \nu) = \begin{cases} \varphi(\nu) & \text{for} \quad |\mathbf{x} - \mathbf{x}_i| \leq r_s \\ 0 & \text{for} \quad |\mathbf{x} - \mathbf{x}_i| > r_s \end{cases} . \tag{63}$$

The function $\varphi(\nu)$ is the Doppler profile defined in Eq. (25).

In general, the finite element code is able to consider arbitrary velocity fields. For velocity fields defined on a discrete grid, e.g. resulting from hydrodynamical simulations, the velocity gradient in direction $\mathbf{n}$ must be obtained numerically. Here, we use two simple velocity fields and calculate the function w analytically.

The first velocity field describes a spherically symmetric collapsing ($v_0 < 0$) or expanding ($v_0 > 0$) medium and is of the form

$$\mathbf{v}_{\mathrm{io}} = v_0 \left(\frac{r_0}{r}\right)^l \frac{\mathbf{x}}{r}, \tag{64}$$

where $r = |\mathbf{x}|$ and v_0 the scalar velocity at radius r_0. The corresponding w function is

$$w(\mathbf{x}, \mathbf{n}) = v_0 \left(\frac{r_0}{r}\right)^l \left(\frac{1}{r} - (l+1)\frac{|\mathbf{nx}|}{r^3}\right). \tag{65}$$

For the second velocity field, we assume rotation around the z-axis

$$\mathbf{v}_{\mathrm{rot}} = v_0 \left(\frac{R_0}{R}\right)^l R^{-1} \begin{pmatrix} y \\ -x \\ 0 \end{pmatrix}, \tag{66}$$

where $R^2 = x^2 + y^2$ is the distance from the rotational axis and v_0 the scalar velocity at distance R_0. For $\mathbf{n} = (n_x, n_y, n_z)$, the w function reads

$$w = v_0 \left(\frac{R_0}{R}\right)^l (l+1) \left(\frac{xy(n_y^2 - n_x^2) + n_x n_y (x^2 - y^2)}{R^3}\right). \tag{67}$$

Fig. 1 shows the results of the finite element code for different optical depths, velocity fields and redistribution functions. We used 41 frequencies equally spaced in the interval $(\nu - \nu_0)/\Delta\nu_D = [-4, 6]$ and 80 directions. Starting with a grid of 4^3 cells and a pre-refined source region, we needed 3–5 spatial refinement steps.

For the simplest case of a static model configuration with coherent isotropic scattering even analytical solutions exist (see [RM01]). Fig. 1a displays the

Table 2. *Parameters used for all calculations. Distances are given in units of the computational unit cube.*

r_h	r_c	α	r_s	v_D	v_0	r_0	R_0
1.0	0.2	10^3	0.2	$10^{-3}c$	$-10^{-3}c$	0.2	1.0

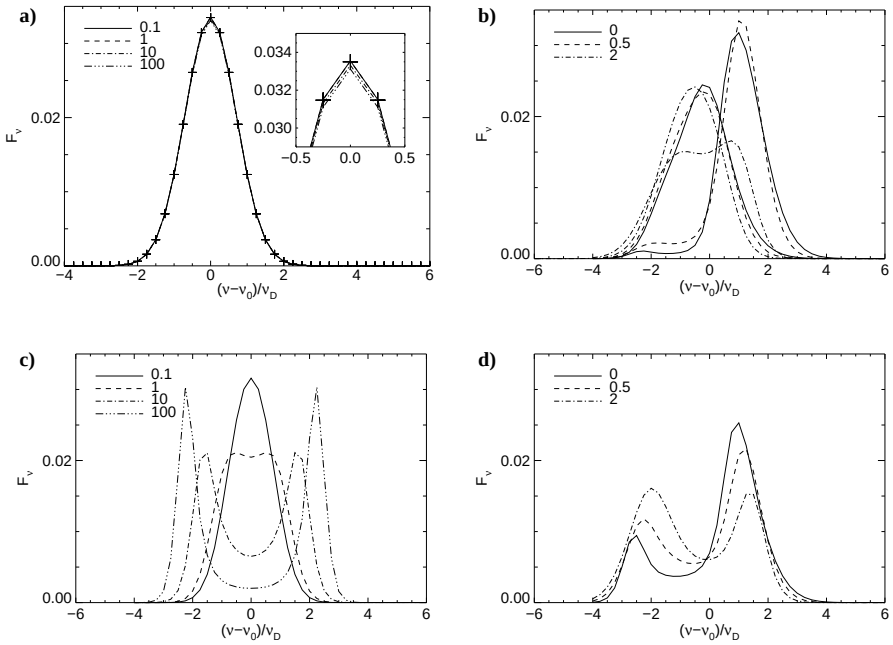

Fig. 1. *Lyα line profiles calculated with the finite element code for a spherically symmetric model configuration: a) a static halo with coherent scattering, b) an collapsing halo with coherent scattering, c) a static halo with complete redistribution, and d) an collapsing halo with complete redistribution. For the static cases a) and c) the line styles refer to calculations with different optical depth τ as indicated. The small window in a) enlarges the peak of the line. The crosses mark the results of the analytical solution. For the moving halos we show in b) the results for $\tau = 1$ (thin lines) and $\tau = 10$ (thick lines) and in d) only for $\tau = 10$. Here, the line styles refer to the exponent l used for the velocity fields.*

line profiles for different τ. As expected, the Doppler profile is preserved and the flux F_ν is independent on τ. The deviation of the numerical results from the analytical solution indicated with crosses is very small. The line profiles for $\tau = 0.1$ and $\tau = 1$ are identical even in the little window which shows the peak of the line in more detail. For $\tau = 100$, the total flux is still conserved better than 99%. This result demonstrates that the frequency-dependent version of our finite element code works correctly.

Next, we consider a collapsing halo with coherent scattering and show the effects of frequency coupling due to the Doppler term. The line profiles in Fig. 1b are plotted for different exponents l of the velocity field $\mathbf{v}_{\rm io}$ defined in Eq. (64). The line profiles are redshifted for $\tau = 1$ (thin lines). Most of the photons directly travel through the part of the halo moving away from the observer. Since the Doppler term is proportional to the gradient of the velocity field, the redshift is larger for a greater exponent l. For $\tau = 10$ (thick lines), the line profiles are blueshifted. Before photons escape from the optically thick part of the halo in front of the source, they are back-scattered and blueshifted in the approaching part of the halo behind the source. The blueshift is less pronounced for the accelerated inflow with $l = 2$, because the strong gradient of the velocity field leads to a slight redshift in the very inner parts of the halo. In this region, the total optical depth is still small. Further out, where the total optical depth increases, the line profile becomes blueshifted.

Complete redistribution leads to an even stronger coupling than the Doppler effect (see Sect. 3). The line profiles obtained for a static model with complete redistribution are displayed in Fig. 1c for different τ. With increasing optical depth the photons more and more escape through the line wings. For $\tau \geq 1$, we get a double-peaked line profile with an absorption trough in the line center. The greater τ the larger the distance between the peaks and the depth of the absorption trough. Since our frequency resolution is too poor for the narrow wings, the flux conservation is only 96% for $\tau = 100$.

Fig. 1d shows the results for an collapsing halo with complete redistribution for $\tau = 10$ and different exponents l. For $l = 0$ and $l = 0.5$ the collapsing motion of the halo enhances the blue wing of the double-peaked line profile. Equally, an expanding halo would enhance the red peak. But for $l = 2$, the red peak is slightly enhanced for an collapsing halo due to the strong velocity gradient, as explained above. This example allows an insight into the mechanisms of resonance line formation and shows the necessity of a profound multidimensional treatment.

7 Applications

All calculations discussed in this section were performed with complete redistribution. We used 49 equidistant frequencies covering the interval $(\nu - \nu_0)/\Delta\nu_D = [-6, 6]$, 80 directions and started from a grid with 4^3 cells and pre-refined source regions, which results in several 10^3 cells for the initial mesh. 3–7 refinement steps were performed leading to approximately 10^5 cells for the finest grid.

7.1 Elliptical Halos

As a first step towards a full three-dimensional problem without any symmetries, we investigated an axially symmetric, disk-like model configuration with

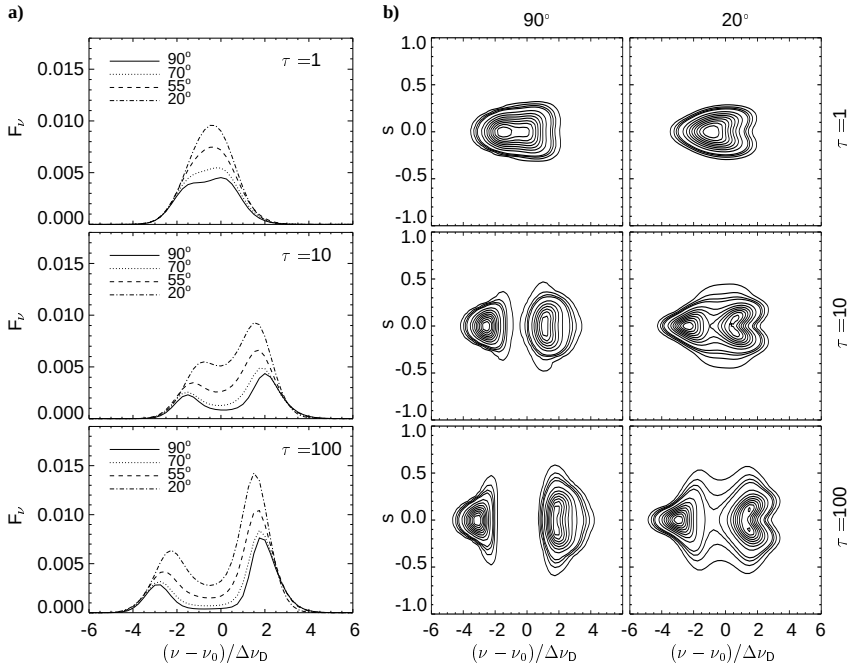

Fig. 2. *Results obtained for a disk-like model configuration with global inflow motion ($l = 0.5$): a) Line profiles for different viewing angles and optical depths $\tau = \tau(\mathbf{n}_{\rm thick})$. b) Two-dimensional spectra for an edge-on view (90°) and a nearly face-on view (20°) and different optical depths. The parameter s gives the spatial position within a slit covering the "visible" part of the disk-like halo. The contours are given for 2.5%, 5%, 7.5%, 10%, 20%, ..., 90% of the maximum value.*

$r^2 = (x/3)^2 + (y/3)^2 + z^2$ in Eq. (61), and with a single source located at $\mathbf{x} = 0$ for several $\tau = \tau(\mathbf{n}_{\rm thick})$ and for different velocity fields. The most optically thick direction $\mathbf{n}_{\rm thick}$ is the direction within the equatorial plane of the disk. The direction perpendicular to the equatorial plane is the z-axis which we also call rotational axis even for cases without rotation.

First, we consider an inflow velocity field with $l = 0.5$ suitable for a gravitational collapse. Fig. 2a displays the calculated line profiles for different τ and viewing angles. As expected, the blue peak of the line is enhanced. The higher τ the stronger the blue peak. Two-dimensional spectra from high-resolution spectroscopy provide frequency-dependent data for only one spatial direction. This is achieved using so-called slit masks for telescope observations. In order to compare our results with these observations we calculated two-dimensional spectra in Fig. 2b using the data within a slit covering the "visible" part of the disk-like halo, i.e. the observable spatial distribution of the frequency integrated intensity. For low optical depth, the shape of the contour lines is a triangle. Photons changing frequency in order to escape via the blue wing

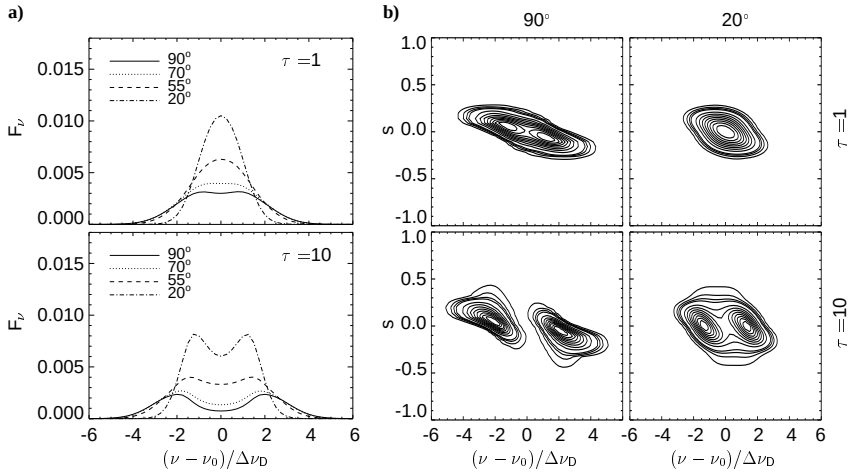

Fig. 3. *Results obtained for a disk-like model configuration with Keplerian rotation ($l = 0.5$) around the z-axis: a) Line profiles for different viewing angles and optical depths $\tau = \tau(\mathbf{n}_{\rm thick})$. b) Two-dimensional spectra for an edge-on view (90°) and a nearly face-on view (20°) and different optical depths. The parameter s gives the spatial position within a slit covering the "visible" part of the disk-like halo. The contours are given for 2.5%, 5%, 7.5%, 10%, 20%, ..., 90% of the maximum value.*

are also scattered in space. The consequence is the greater spatial extent of the blue wing. Apart from a growing gap between the two peaks with higher optical depth, the general triangular shape in conserved.

Next, we investigated the disk-like model configuration with Keplerian rotation ($l = 0.5$), where the z-axis is the axis of rotation. The results are plotted in Fig. 3 for $\tau = 1$ and $\tau = 10$. The calculated line profiles appear to be symmetric with respect to the line center and show the same behavior with increasing optical depths as in the static case. However, the extension of the line wings towards higher and lower frequencies is strongly increasing with increasing viewing angle because of the growing effect of the velocity field. Rotation is clearly visible in the two-dimensional spectra (Fig. 3b). The shear of the contour lines is the characteristical pattern indicating rotational motion. For an edge-on view at $\tau = 10$, Keplerian rotation produces two banana-shaped emission regions.

Finally, Fig. 7.1 depicts the spatial intensity distribution for particular frequency points within the interval $(\nu - \nu_0)/\Delta\nu_D = [-2, +2]$ (rows) and for different viewing angles (columns). The left figure shows the results obtained for a disk-like model configuration with global inflow motion ($l = 0.5$). The right figure shows the results obtained for a disk-like model configuration with Keplerian rotation ($l = 0.5$) around the z-axis. The intensity increases from blue to white.

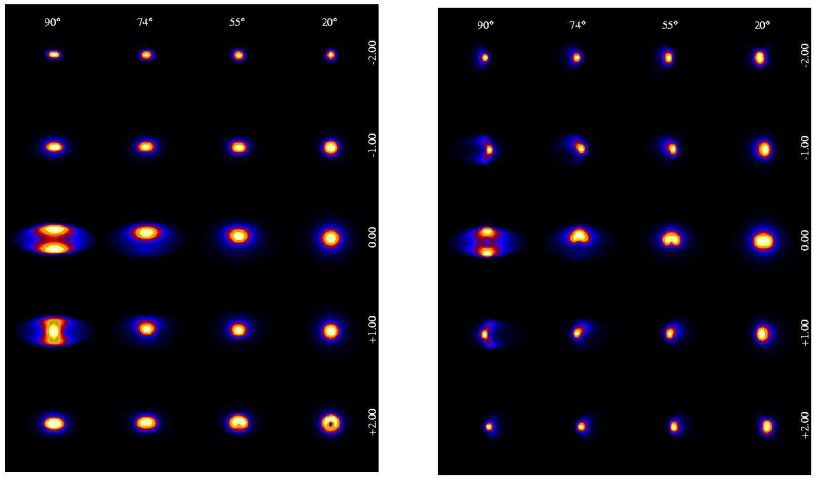

Fig. 4. *Spatial intensity distribution for particular frequency points within the interval* $(\nu - \nu_0)/\Delta\nu_D = [-2, +2]$ *(rows) and for different viewing angles (columns).* Left: *Results obtained for a disk-like model configuration with global inflow motion* ($l = 0.5$)*.* Right: *Results obtained for a disk-like model configuration with Keplerian rotation* ($l = 0.5$) *around the z-axis. The intensity increases from blue to white.*

In spite of the relatively low optical depth of the simple model configurations, our results reflect the form of line profiles and the patterns in two-dimensional spectra of many high redshift galaxies. For example, the two-dimensional spectra of the Lyα blobs published in [SAS00] (see Fig. 8) are comparable to the results obtained for collapsing (Fig. 2b) and rotating (Fig. 3b) halos. In the sample presented in [ORM97] are many high redshift radio galaxies with single-peaked and double-peaked Lyα profiles. The corresponding two-dimensional spectra show asymmetrical emission regions which are more or less extended in space. The statistical study of emission lines from high redshift radio galaxies in [BRM00] indicates that the triangular shape of the Lyα emission is a characteristical pattern in the two-dimensional spectra of high redshift radio galaxies. Since the emission of the blue peak of the line profile is predominately less pronounced, most of the associated halos should be in the state of expansion.

7.2 Multiple Sources

High redshift radio galaxies are found in the center of proto clusters. In such an environment, it could be possible that the Lyα emission of several galaxies is scattered in a common halo. To investigate this scenario, we started with a spherically symmetric distribution for the extinction coefficient and with

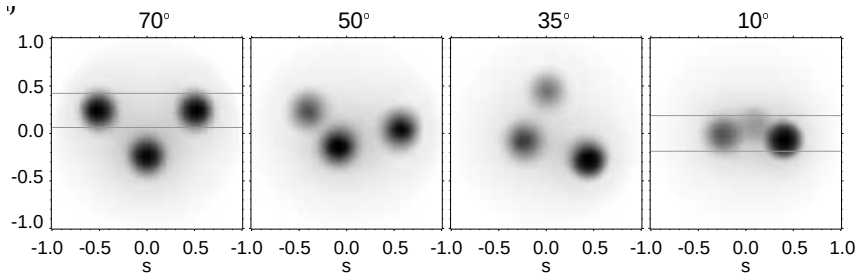

Fig. 5. *Spatial distribution of the frequency integrated intensity for a static spherically symmetric halo configuration with* $\tau = 10$ *and three source regions for different viewing angles. The slit position is indicated for two different viewing angles (for details see text).*

three source regions located at $x_1 = [0.5, 0.25, 0]$, $x_2 = [-0.5, 0.25, 0]$ and $x_3 = [0, -0.25, 0]$ forming a triangle in the x-y-plane. In the following figures, the results for $\tau = 10$ are presented.

Figure 5 shows Lyα images for four selected viewing directions. The specified angle is the angle between the viewing direction and the x-y-plane. Note that the orientation of the source positions within the plane is different for each image. Viewing the configuration almost perpendicular to the x-y-plane (70°), renders all three source regions visible, because the source regions are situated in the more optically thin, outer parts of the halo. Remember that most of the scattering matter is in and around the center of the system. For other angles, some of the source regions are located behind the center and therefore less visible on the images.

The corresponding line profiles and two-dimensional spectra are displayed in Fig. 6 for the static case as well as for a halo with global inflow and Keplerian rotation. Two-dimensional spectra from high-resolution spectroscopy provide frequency-dependent data for only one spatial direction. This is achieved using so-called slit masks for telescope observations. In order to compare our results with these observations we calculated two-dimensional spectra using the data within a slit covering the most "visible" parts of the halo, i.e. as many observable source regions as possible. Width and position of the slits are depicted in Fig. 5. We get double-peaked line profiles for almost all cases, except for the rotating halo, where the line profiles are very broad for viewing angles lower than 70°. Additional features, dips or shoulders, are visible in the red or blue wing. They arise because the three sources have significantly different velocities components with respect to the observer.

The slit for a viewing angle of 70° contains two sources. They show up as four emission regions in the two-dimensional spectra (Fig. 6b). The pattern is very symmetric, even for the moving halos. For a viewing angle of 10°, the slit covers all source regions. Nevertheless, the two-dimensional spectra are dominated by two pairs of emission regions resulting from the sources

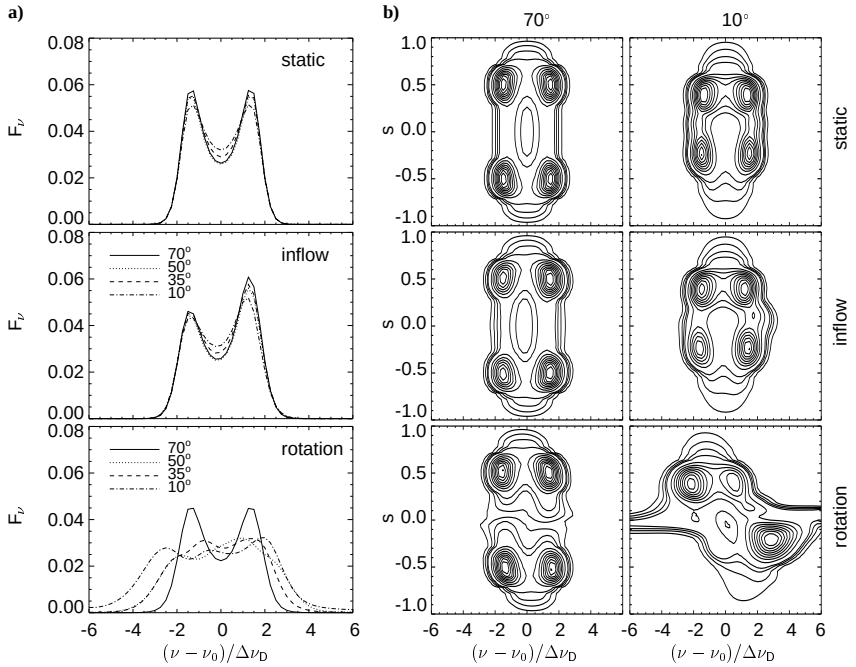

Fig. 6. *Results obtained for a spherically symmetric halo configuration with $\tau = 10$ and three source regions for the static case and two different velocity fields (inflow and rotation): a) Line profiles for different viewing angles. b) Two-dimensional spectra for a nearly face-on view (70°) and a nearly edge-on view (10°). The position and width of the slit is indicated in Fig. 5. The contours are given for 2.5%, 5%, 7.5%, 10%, 20%, ..., 90% of the maximum value.*

located closer to the observer. The third source region only shows up as a faint emission in the blue part in the case of global inflow. In the case of rotation, emission regions from a third source are present. But the overall pattern is very irregular and prevents a clear identification of the emission regions.

Finally, Fig. 7.2 depicts the spatial intensity distribution for particular frequency points within the interval $(\nu - \nu_0)/\Delta\nu_D = [-2, +2]$ (rows) and for different viewing angles (columns). The left figure shows the results obtained for a spherically symmetric halo configuration with $\tau = 10$ and three source regions for global inflow motion. The right figure shows the results obtained for a spherically symmetric halo configuration with $\tau = 10$ and three source regions for Keplerian rotation around the z-axis. The intensity increases from blue to white.

This example demonstrates the complexity of three dimensional problems. In a clumpy medium, the determination of the number and position of Lyα sources would be difficult by means of frequency integrated images alone.

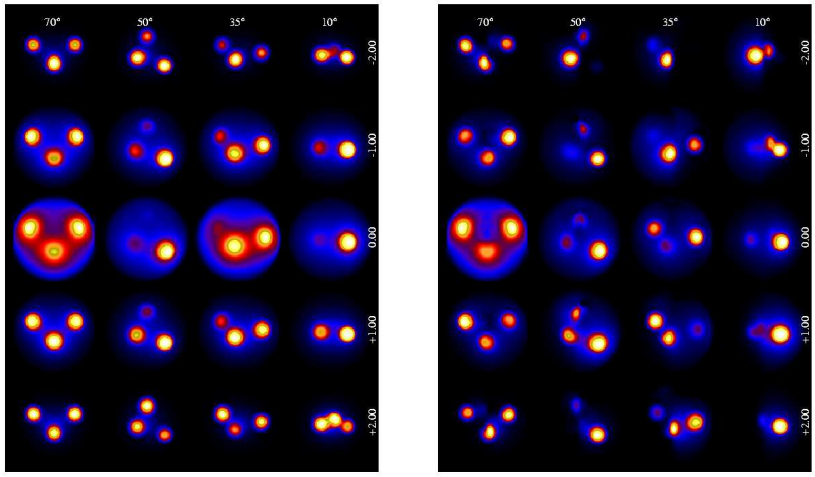

Fig. 7. *Spatial intensity distribution for particular frequency points within the interval* $(\nu - \nu_0)/\Delta\nu_D = [-2, +2]$ *(rows) and for different viewing angles (columns).* Left: *Results obtained for a spherically symmetric halo configuration with* $\tau = 10$ *and three source regions for global inflow motion.* Right: *Results obtained for a spherically symmetric halo configuration with* $\tau = 10$ *and three source regions for Keplerian rotation around the z-axis. The intensity increases from blue to white.*

Two-dimensional spectra may help, but could prove to be too complicated. More promising are images obtained from different parts of the line profile or information from other emission lines of OIII or Hα in a manner proposed in [KPR02].

8 Multi-Model Preconditioning

It is often necessary to solve radiation transfer problems in composite domains with mixed transport regimes, so that in some parts of the domain there is diffusion control, whereas radiative transfer dominates elsewhere. The character of the transfer changes strongly, giving a change in the type of equation, if diffusion control changes to radiation control. In case of such a mixed regime, therefore, the application of standard solvers and of standard preconditioning methods for the discrete problem is usually marred by an extremely slow rate of convergence. In this section, we propose a solution method combining the radiative transfer model with its diffusion approximation, which is designed to yield good convergence rates for both types of the equation. For various reasons, the diffusion approximation alone is not sufficient, and the more general radiation transfer equation must be solved. First, we do not assume a

lower bound for the scattering cross section and, therefore, the approximation may become inaccurate in parts of the domain. Furthermore, the question arises as to what boundary conditions for the diffusion problem are physically acceptable. These problems can be fully resolved only by solving the radiative transfer equation. Since the spectrum of the discrete operator becomes degenerate in the limit when scattering dominates, the solution of the corresponding discrete linear system is particularly challenging (see [Kan96]).

When the parameters of the equation are constant, efficient solution techniques can be found easily. If scattering is small, a simple Gauss-Seidel process yields good convergence rates (see [JP86]). In the limit of high scattering, the solution is isotropic in the interior of the domain yielding an elliptic second order equation, which can be solved efficiently using multilevel preconditioning. The scheme suggested in this section combines these two preconditioners in a way related to two-level multigrid algorithms. It exploits the good convergence properties of both methods in different regimes. Similar schemes have been proposed under the names of quasi diffusion and diffusion-synthetic acceleration method (for details see [Lar91, AL02] and the literature cited therein).

8.1 Discretization and Diffusion Approximation

Let us first consider monochromatic radiative transfer problems and rewrite the corresponding partial integro-differential equation (2) for a multidimensional spatial domain $\Omega \subset \mathrm{R}^d$ $(d = 2, 3)$

$$\mathbf{n} \cdot \nabla_x I(\mathbf{x}, \mathbf{n}) = -\chi(\mathbf{x}) \Big(I(\mathbf{x}, \mathbf{n}) - \frac{1-\epsilon}{2(d-1)\pi} \int\limits_{S^{d-1}} I(\mathbf{x}, \mathbf{n}')\, d\omega' - \epsilon f(\mathbf{x}) \Big), \quad (68)$$

with the thermalization factor $\epsilon = \kappa/\chi$ and the albedo $1 - \epsilon = \sigma/\chi$. For the sake of simplicity, isotropic scattering (i.e., phase function $P(\mathbf{n}', \mathbf{n}) \equiv 1$), a constant source function $f(\mathbf{x}) = 1$ and – if not stated otherwise – zero boundary conditions are adopted. The test calculations which follow are exclusively performed for 2D configurations (i.e., $d = 2$). For the discretization of the integral operator in (68), a collocation method is used, again as described in Sect. 4.2, using a set of equally spaced points on the unit circle. Then, the transport equation (68) gives for an arbitrary fixed direction $\mathbf{n}_i$

$$\mathbf{n}_i \cdot \nabla_x I(\mathbf{x}, \mathbf{n}_i) + \chi(\mathbf{x}) I(\mathbf{x}, \mathbf{n}_i) = \chi(\mathbf{x}) \Big((1-\epsilon) \sum_{k=1}^{k=m} \omega_{ik} I(\mathbf{x}, \mathbf{n}_k) + \epsilon f(\mathbf{x}) \Big), \quad (69)$$

where the ω_{ik} are suitable quadrature weights with $\sum_k \omega_{ik} = 1$. Equation (69) is discretized by the discontinuous Galerkin finite element method (DGFEM) proposed for neutron transport without scattering in [LR74] and for radiative transfer problems in [KM04]. Let $\mathbb{T}_h$ be a mesh of quadrilaterals K covering the domain Ω exactly. On $\mathbb{T}_h$ the finite element space V_h used for the specific intensity is defined by

$$V_h = \left\{ v \in L^2(\mathbb{T}_h) \,\middle|\, v|_K \in \mathcal{P},\ \forall K \in \mathbb{T}_h \right\}. \tag{70}$$

$\mathcal{P}$ is either the space of polynomials of degree k or the space of isoparametric tensor product polynomials of degree k on K. We assume $k \geq 1$, yielding a discretization of second order at least.

At large optical depths ($\chi \gg 1$) radiative transfer in scattering dominated media ($\epsilon \to 0$) becomes simple because all scale lengths become larger than the photon mean free path length ($\sim 1/\chi(\mathbf{x})$). Simple approximations to this transport problem, based either on ad hoc physical assumptions such as Fick's law (cf. [Lam65, DL00]) or on a polynomial approximation, which assumes that the flux has an expansion into the first two Legendre Polynomials (cf. [CZ67]), result in a diffusion equation

$$-\nabla_x \cdot \left(\frac{1}{d\,\chi} \nabla_x J(\mathbf{x}) \right) + \kappa J(\mathbf{x}) = \kappa f(\mathbf{x}) \tag{71}$$

for the mean intensity $J(\mathbf{x}) = 1/(2(d-1)\pi) \int_{s^2} I(\mathbf{x}, \mathbf{n}) d\omega$. Usually, fixed boundary conditions of the type $J(\mathbf{x}) = g(\mathbf{x})$ are posed on the spatial boundary surface Γ. To derive the basic asymptotic (diffusion) limit for scattering dominant, optically thick transport problems, the point $\mathbf{x}$ under consideration must be far from the boundary (optical depth $\tau \gg 1$) and far from the zones of the domain Ω where the coefficients κ and σ vary strongly. In the 1970s and 1980s, the mathematical relationship between transport and diffusion theory has been clarified in a large body of work showing that transport theory transitions into diffusion theory in a certain asymptotic limit. A sampling of this work is given in [LK74, HM75, Pap75, LPB83, LMM87]. As for the radiative transfer equation (69) the DGFEM discretization of the diffusion equation (71) is achieved by the (symmetric) interior penalty method due to [Arn82] with polynomials of degree $k \geq 1$, yielding a discretization of second-order at least. The linear system of equations resulting from the DGFEM discretization of Eq. (68) has the block structure

$$\mathbf{A}_{\text{diff}}\, \mathbf{J} = \mathbf{f}. \tag{72}$$

$\mathbf{J}$ is the vector of discrete mean intensities and $\mathbf{f}$ is any given data (thermal radiation and boundary data). The $(n \times n)$-matrix $\mathbf{A}_{\text{diff}}$ corresponds to the DGFEM discretization of the left hand side of Eq. (71).

8.2 Preconditioning

The linear system of equations resulting from the DGFEM discretization of Eq. (68) has the block structure

$$\left(\begin{pmatrix} A_1 & & \\ & \ddots & \\ & & A_M \end{pmatrix} - \begin{pmatrix} \omega_{11}X & \cdots & \omega_{1M}X \\ \vdots & & \vdots \\ \omega_{M1}X & \cdots & \omega_{MM}X \end{pmatrix} \right) \begin{pmatrix} u_1 \\ \vdots \\ u_M \end{pmatrix} = \begin{pmatrix} f_1 \\ \vdots \\ f_M \end{pmatrix}. \tag{73}$$

Here, u_i is the vector of discrete intensities and f_i is any given data (thermal radiation and boundary data) for any fixed direction $\mathbf{n}_i$ $(i = 1, \ldots, M)$. Each $(n \times n)$-matrix A_i corresponds to the DGFEM discretization of the left hand side of Eq. (69) for a single radiation direction $\mathbf{n}_i$ and X discretizes the multiplication with $(1 - \epsilon)\chi$. The operator form of Eq. (73) reads

$$\mathbf{A}_{\mathrm{rte}}\, \mathbf{u} = \mathbf{f}, \tag{74}$$

where $\mathbf{A}_{\mathrm{rte}} = \mathbf{T} - \mathbf{S}$ is the pure transport operator $\mathbf{T}$ minus the scattering operator $\mathbf{S}$.

Given a system of linear equations (74) and an iterate $\mathbf{u}^i$, the *iteration error* is defined as

$$\mathbf{e}^i := \mathbf{u} - \mathbf{u}^i. \tag{75}$$

An equation for the error is given by the defect equation

$$\mathbf{A}_{\mathrm{rte}}\, \mathbf{e}^i = \mathbf{A}_{\mathrm{rte}}\, \left(\mathbf{u} - \mathbf{u}^i\right) = \mathbf{f} - \mathbf{A}_{\mathrm{rte}}\, \mathbf{u}^i = \mathbf{d}^i. \tag{76}$$

An approximation $\mathbf{g}(\mathbf{x}, \mathbf{n})$ for $\mathbf{e}^i$ can be computed by solving

$$\mathbf{M}\, \mathbf{g} = \mathbf{d}^i \qquad \Longleftrightarrow \qquad \mathbf{g} = \mathbf{M}^{-1} \left(\mathbf{f} - \mathbf{A}_{\mathrm{rte}}\, \mathbf{u}^i\right). \tag{77}$$

$\mathbf{M}$ should be an approximation of $\mathbf{A}_{\mathrm{rte}}$ that is easy to invert, such as:

$\mathbf{M}$ identity matrix	(Richardson method)
$\mathbf{M}$ diagonal of $\mathbf{A}_{\mathrm{rte}}$	(Jacobi method)
$\mathbf{M}$ lower triangle of $\mathbf{A}_{\mathrm{rte}}$	(Gauss-Seidel method).

Now a new iterate is obtained by

$$\mathbf{u}^{i+1} = \mathbf{u}^i + \mathbf{g}. \tag{78}$$

Renumbering the degrees of freedom according to the photon transport direction $\mathbf{n}_i$, the matrices A_i in Eq. (73) can be inverted easily by a front solving algorithm (see [JP86]). Therefore, a simple, well-known preconditioner for the system (73) is the matrix

$$\mathbf{\Lambda} = \begin{pmatrix} A_1^{-1} & & \\ & \ddots & \\ & & A_M^{-1} \end{pmatrix}. \tag{79}$$

It is this preconditioner, that is used in the well-known Λ- or Source Iteration method. Thus, with $\mathbf{M} \equiv \mathbf{\Lambda}$ the new iterate in Eq. (78) reads

$$\mathbf{u}^{i+1} = \mathbf{\Lambda} \left(\mathbf{f} + \begin{pmatrix} \omega_{11} X & \cdots & \omega_{1M} X \\ \vdots & & \vdots \\ \omega_{M1} X & \cdots & \omega_{MM} X \end{pmatrix} \mathbf{u}^i \right). \tag{80}$$

Table 3. *GMRES steps required for the reduction of residual by a factor of* 10^{-5} *for constant coefficients using the preconditioner* Λ.

χ	0.10	1	10	10^2	10^3	10^4
ϵ	0.91	0.1	10^{-2}	10^{-4}	10^{-6}	10^{-8}
cells						
256	2	5	15	88	423	1424
1024	2	5	16	108	1427	4929
4096	2	5	16	122	2871	13759
16384	2	5	17	131	4718	—

This preconditioner performs well only if the extinction χ is small or the albedo $1-\epsilon$ is bounded away from 1. It can be enhanced by replacing the blocks A_i in $\mathbf{\Lambda}$ by $A_i - \omega_{ii}X$ (cf. [Kan96, Tur93]). Still, this version suffers from the same limitations as the Λ-preconditioner in the case of dominant scattering. In fact, acceleration methods for the Λ- or Source Iteration method that are based on matrix algebra, such as Jacobi and Gauss-Seidel preconditioning, have not proved to be as useful as methods based on direct manipulation of the transport equation itself. This latter class of methods is described in great detail in [Lar91, AL02].

We are now going to formulate a preconditioning scheme for the more general radiation transport problem in Eq. (74), which uses the solution of the diffusion problem in Eq. (72) to improve the extremely poor convergence for configurations which are optically thick and dominated by scattering. Transport-dominated problems are also solved by the preconditioning front-solving algorithm described above, which performs efficiently. The scheme suggested here combines these two preconditioners in a way related to two-level multigrid algorithms (see [Hac85]). It exploits the good convergence properties of both methods in different regimes. The general framework of a two-level multigrid algorithm places much of the earlier work on transport acceleration methods described in [AL02] in a common, unified framework (for details see [Lar91]). For such algorithms, one has a "fine mesh" on which the original problem defined in Eq. (74) is to be solved, and a "coarse mesh" on which "corrections" to the transport iterative solution are obtained (cf. Eq. (72)). The word "multigrid" often connotes a sequence of increasingly coarse spatial meshes. However, for transport problems, space and angle are variables, and the method we consider involves "collapsing" the transport problem onto "coarser grids" independent of the photon direction. Since only two "grids" are used, the framework of a two-level multigrid algorithm is adequate, for which we propose the acronym MMP, which stands for multi-model preconditioner.

In comparison to standard Λ- or Krylov-type iteration methods with acceleration by Jacobi or Gauss-Seidel preconditioning, our MMP algorithm is designed to give less of an iteration error $\mathbf{e}^i$ as defined by Eq. (75), while requiring a significantly smaller number of iteration steps. Like any other two-level multigrid method, our MMP algorithm combines the smoothing op-

eration in Eq. (80) with a "coarse grid" correction, which is obtained from solving the diffusion problem defined in Eq. (72). When this is done, the vector $\mathbf{d}^i(\mathbf{x},\mathbf{n})$ can be composed, which is the defect iterate of the discretized radiation transport problem (cf. Eq. (74)–(77)). The MMP method then employs the following succession of steps:

1. "fine grid" pre-smoothing by transport preconditioner $\mathbf{\Lambda}$

$$\mathbf{g}_1(\mathbf{x},\mathbf{n}) = \mathbf{\Lambda}\,\mathbf{d}^i(\mathbf{x},\mathbf{n}), \tag{81}$$

2. projection of "fine grid" residual to "coarse grid" (restriction)

$$\bar{\mathbf{g}}_2(\mathbf{x}) = \frac{1}{2\pi(d-1)} \int\limits_{S^{d-1}} (\mathbf{d}^i(\mathbf{x},\mathbf{n}) - \mathbf{A}_{\mathrm{rte}}\,\mathbf{g}_1(\mathbf{x},\mathbf{n}))\,d\omega \tag{82}$$

3. "coarse grid" solution of diffusion problem (cf. Eq. (72))

$$\mathbf{A}_{\mathrm{diff}}\,\bar{\mathbf{g}}_3(\mathbf{x}) = \bar{\mathbf{g}}_2(\mathbf{x}) \tag{83}$$

4. "coarse grid" correction (prolongation)

$$\mathbf{g}_4(\mathbf{x},\mathbf{n}_j) = \mathbf{g}_1(\mathbf{x},\mathbf{n}_j) + \bar{\mathbf{g}}_3(\mathbf{x}) \qquad \forall \text{ directions } j = 1,\ldots,M \tag{84}$$

5. "fine grid" post-smoothing by transport preconditioner $\mathbf{\Lambda}$

$$\mathbf{g}_5(\mathbf{x},\mathbf{n}) = \mathbf{g}_4(\mathbf{x},\mathbf{n}) + \mathbf{\Lambda}\left(\mathbf{d}^i(\mathbf{x},\mathbf{n}) - \mathbf{A}_{\mathrm{rte}}\,\mathbf{g}_4(\mathbf{x},\mathbf{n})\right). \tag{85}$$

The accuracy of the high-frequency eigenvectors improves due to error reduction by what is known as the smoothing property of the iteration (for details see [Hac85]). These high-frequency eigenvectors are determined by the local part of the transfer operator $\mathbf{A}_{\mathrm{rte}}$, i.e. they arise from pure transport and absorption. The idea of the MMP scheme is to construct an iteration that is complementary to the smoother, so that a reduction in the error for the low-frequency eigenvectors is obtained. These errors are determined by the non-local part of the transfer operator, i.e., they arise from the scattering contribution to $\mathbf{A}_{\mathrm{rte}}$. A reduction of the low-frequency errors can be obtained from using a "coarser grid", so that less computational effort is needed.

8.3 Numerical Results

We test the performance of the multi-model preconditioner with a model problem on the unit square $\Omega = [-1,1]^2$ that uses constant coefficients χ and ϵ on the whole domain.

All MMP examples are computed using the GMRES method with right preconditioning and, therefore, convergence is measured by the norm of the original residual, not the preconditioned one. Table 3 and 4 display the number of iteration steps required to reduce the Euclidean norm of the initial

Table 4. *GMRES steps required for the reduction of residual by a factor of* 10^{-5} *for constant coefficients using the exact MMP preconditioner.*

χ	0.10	1	10	10^2	10^3	10^4
ϵ	0.91	0.1	10^{-2}	10^{-4}	10^{-6}	10^{-8}
cells						
256	2	4	7	12	24	26
1024	2	4	7	10	21	24
4096	2	4	7	9	16	23
16384	2	4	7	8	14	24

Table 5. *Computation time [sec] required to reduce the residual by a factor of* 10^{-5}.

χ	0.10	1	10	10^2	10^3	10^4
ϵ	0.91	0.1	10^{-2}	10^{-4}	10^{-6}	10^{-8}
cells	only Λ preconditioner					
4096	0.5	1.3	4.8	103	3319	16457
16384	2.6	7.4	23.5	—	—	—
	exact MMP preconditioner					
4096	4.5	7.2	13	15	24.5	36.7
16384	19.4	33	55.3	62.6	104	181.5

residual by a factor of 10^{-5}. Since one smoothing step is sufficient for the MMP method, only the post-smoothing in Eq. (85) is applied. The results displayed in Table 4 show clearly that the number of iteration steps depends only moderately on the extinction coefficients and the thermalization parameters, which was the primal goal. In particular, these numbers are considerably smaller than the ones reported for the Λ-iteration as preconditioner in Table 3. There, the GMRES method was restarted every 150 steps; we chose such a large basis size to ensure a fair comparison.

Since Eq. (71) gives a good approximation to the radiative transfer problem in regions with dominant scattering, this is not true in the transport dominated case. Moreover, the model problem we consider contains parts where $\chi(\mathbf{x}) = 0$. In order to solve Eq. (71), we define a cut-off $\widehat{\chi}$ and replace $\chi(\mathbf{x})$ by $\max\{\widehat{\chi}, \chi(\mathbf{x})\}$. The results in this section show that this is a feasible approach. Having this modification in mind, we use χ throughout the paper in order not to confuse the notation.

Since the two preconditioners, Λ and exact MMP require different amounts of work in each iteration step, the number of steps required is not sufficient for an assessment of their efficiency. Therefore, we compare computation times for the two schemes in Table 5. The longer computation times for the Λ-preconditioner on the finer grid are missing, because the large basis chosen required a bigger machine with different runtime characteristics. Still, the tables show that the exact MMP preconditioner is not much slower when not needed (a factor of about 5 per step), while it clearly outperforms the Λ-method for diffusive problems.

9 Summary

A finite element code for solving the resonance line transfer problem in moving media is presented. Simple velocity fields and complete redistribution are considered. The code is applicable to any three-dimensional model configuration with optical depths up to 10^3–10^4.

The application to the hydrogen Lyα line originating from slightly optically thick model configurations ($\tau \leq 10^2$) are shown and the resulting line profiles are discussed in detail. The systematic approach from very simple to more complex models gave the following results:

- An optical depth of $\tau \geq 1$ leads to the characteristic double peaked line profile with a central absorption trough as expected from analytical studies (e.g., see [Neu90]). This form of the profile is the result of scattering in space and frequency. Photons escape via the line wings where the optical depth is much lower.
- Global velocity fields destroy the symmetry of the line profile. Generally, the blue peak of the profile is enhanced for models simulating a collapse motion and the red peak for expanding media. But there are certain velocity fields (e.g. with steep gradients) and spatial distributions of the extinction coefficient, where the formation of a prominent peak is suppressed.
- Double-peaked line-profiles show up as two emission regions in the two-dimensional spectra. Global collapse or expansion leads to an overall triangular shape of the emission. Rotation produces a shear pattern resulting in banana-shaped emission regions for optical depths ≥ 10.
- For non-symmetrical model configurations, the optical depth varies with the line of sight. Thus, the flux, the depth of the absorption trough and the pattern in the two-dimensional spectra strongly depend on the viewing direction.

The applications clearly demonstrate the capacity of the finite element code and show that the three-dimensional structure, the kinematics and the total optical depth of the model configurations are very important. The latter point is crucial, since the convergence of the algorithm is extremely poor for optical depths $\geq 10^3 - 10^4$. These large depths refer to photons at the line center. Photons in the line wings or those emerging close to the boundary of the halo configuration hardly interact with the cold hydrogen gas and will escape almost freely towards the observer. These objects are especially challenging from a numerical point of view. They are simulated by the multi-model preconditioning (MMP) scheme presented in this paper, which combines two distinct preconditioners that are designed to accelerate the solution of transport dominated and highly scattering, optically thick radiative transfer problems. The development of the MMP method was stimulated by the theory of two-level multigrid algorithms which exploit the good convergence properties of both transport and scattering acceleration methods in different

spatial regimes. The monochromatic model problems clearly demonstrate the considerable improvement in run-time efficiency of the MMP scheme.

References

[Ada72] Adams, T.F.: *The escape of resonance-line radiation from extremely opaque media.* Astrophys. J., **174**, 439 (1972)

[AL02] Adams, M.L., Larsen, E.W.: *Fast iterative methods for discrete-ordinates particle transport calculations.* Prog. Nucl. Energy, **40**, No. 1, 3–159 (2002)

[ALL01] Ahn, S.-H., Lee, H.-W., Lee, H. M.: *Lyα line formation in starburst galaxies. I. Moderately thick, dustless and static H I media.* Astrophys. J., **554**, 604–614 (2001)

[ALL02] Ahn, S.-H., Lee, H.-W., Lee, H. M.: *Lyα line formation in starburst galaxies. II. Extremely thick, dustless and static H I media.* Astrophys. J., **567**, 922–930 (2002)

[Arn82] Arnold, D.N.: *An interior penalty finite element method with discontinuous elements.* SIAM J. Numer. Anal., **19**, 742–760 (1982)

[BR01] Becker, R., Rannacher, R.: *An optimal control approach to a posteriori error estimation in finite element methods.* In: Iserles, A. (ed.) Acta Numerica 2001, **37**, p. 1–102, Cambridge University Press (2001) http://www.iwr.uni-heidelberg.de/sfb359/Preprints2001.html

[BBR05] Becker, R., Braack, M., Richter, T.: *Parallel multigrid on locally refined meshes.* In: Rannacher, R. (ed.) Reactive Flows, Diffusion and Transport. Springer, Berlin (2005)

[BKM05] Becker, R., Kapp, H., Meidner, D., Rannacher, R., Vexler, B.: *Adaptive finite element methods for PDE-constrained optimal control problems.* In: Rannacher, R. (ed.) Reactive Flows, Diffusion and Transport. Springer, Berlin (2005)

[Boe96] Böttcher K.: *Adaptive Schrittweitenkontrolle beim Unstetigen Galerkin-Verfahren für Gewöhnliche Differentialgleichungen.* Diploma Thesis, University of Heidelberg (1996)

[BR05a] Braack, M., Richter, T.: *Mesh and model adaptivity for flow problems.* In: Rannacher, R. (ed.) Reactive Flows, Diffusion and Transport. Springer, Berlin (2005)

[BR05b] Braack, M., Richter, T.: *Solving multidimensional reactive flow problems with adaptive finite elements.* In: Rannacher, R. (ed.) Reactive Flows, Diffusion and Transport. Springer, Berlin (2005)

[Bra97] Braess, D.: Finite Elemente. Springer, Berlin (1997)

[BH71] Bramble, J.H.,Hilbert, S.R.: Bounds for a class of linear functionals with applications to Hermite interpolation. Numer. Math., **16**, 362–369 (1971)

[BS96] Brenner, S.C., Scott, L.R.: The Mathematical Theory of Finite Element Methods. Springer, New York (1996)

[CHR05] Carraro, T., Heuvelin, V., Rannacher, R., Waguet, C.: *Determination of kinetic parameters in laminar flow reactors. I. Numerical aspects.* In: Rannacher, R. (ed.) Reactive Flows, Diffusion and Transport. Springer, Berlin (2005)

[CZ67] Case, K.M., Zweiffel, P.F.: *Linear Transport Theory.* Addison-Wesley Publishing Company, Reading, Massachusetts (1967)

[Cia78] Ciarlet, P.G.: The Finite Element Method for Elliptic Problems. North Holland, New York (1978)

[DL00] Dautray R., Lions J.-L.: *Mathematical Analysis and Numerical Methods for Science and Technology.* Vol. 6, Springer, Berlin Heidelberg New York (2000)

[BRM00] De Breuck, C., Röttgering, H., Miley, G., van Breugel, W., Best, P.: *A statistical study of emission lines from high redshift radio galaxies.* Astron. Astrophys., **362**, 519–543 (2000)

[DT00] Dullemond, C.P., Turolla, R.: *An efficient algorithm for two-dimensional radiative transfer in axisymmetric circumstellar envelopes and disks.* Astron. Astrophys., **360**, 1187–1202 (2000)

[ER90] Efstathiou, A., Rowan-Robinson, M.: *Radiative transfer in axisymmetric dust clouds.* Mon. Not. Roy. Astron. Soc., **245**, 275–288 (1990)

[EJT85] Eriksson K., Johnson C., Thomée C.: *Time discretization of parabolic problems by the discontinuous Galerkin method.* RAIRO, Modélisation Math. Anal. Numér., **19**, 611–643 (1985)

[EJ87] Eriksson K., Johnson C.: *Error estimates and automatic time step control for nonlinear parabolic problems. I.* SIAM J. Numer. Anal., **24**, 12–23 (1987)

[EJ91] Eriksson K., Johnson C.: *Adaptive finite element methods for parabolic problems. I: A linear model problem.* SIAM J. Numer. Anal., **28**, 43–77 (1991)

[FK97] Führer C., Kanschat G.: *A posteriori error control in radiative transfer.* Computing, **58**, 317–334 (1997)

[HM91] Haardt, F., Maraschi, L.: *A two-phase model for the X-ray emission from Seyfert galaxies.* Astrophys. J., **380**, L51–L54 (1991)

[HM75] Habetler, G.J., Matkowsky, B.J.: *Uniform asymptotic expansions in transport theory with small mean free paths, and the diffusion approximation.* J. Math. Phys., **16**, 846–854 (1975)

[Hac85] Hackbusch, W.: *Multi-Grid Methods and Applications.* Springer, Heidelberg (1985)

[Hac93] Hackbusch, W.: *Iterative Lösung Grosser Schwachbesetzter Gleichungssysteme.* Teubner, Stuttgart (1993)

[Hog98] Hogerheijde, M.: *The Molecular Environment of Low-Mass Protostars.* Ph.D. Thesis, Rijks Univesiteit Leiden (1998)

[HB82] Hughes, T.J.R., Brooks, A.N.: Streamline upwind/Petrov-Galerkin formulations for convection dominated flows with particular emphasis on the incompressible Navier-Stokes equations. Comput. Methods Appl. Mech. Eng., **32**, 199–259 (1982)

[HK80] Hummer, D.G., Kunasz, P.B.: *Energy loss by resonance line photons in an absorbing medium.* Astrophys. J., **236**, 609–618 (1980)

[Joh87] Johnson, C.: Numerical Solution of Partial Differential Equations by the Finite Element Method. Cambridge University Press, Cambridge (1987)

[JP86] Johnson, C., Pitkäranta, J.: *An analysis of the discontinuous Galerkin method for a scalar hyperbolic equation.* Math. Comput., **46**, 1–26 (1986)

[Juv97] Juvela, M.: *Non-LTE radiative transfer in clumpy molecular clouds.* Astron. Astrophys., **322**, 943–961 (1997)

[Kan96] Kanschat, G.: *Parallel and Adaptive Galerkin Methods for Radiative Transfer Problems.* Ph.D. Thesis, University of Heidelberg (1996) http://www.iwr.uni-heidelberg.de/sfb359/Preprints1996.html

[Kan00] Kanschat, G.: *Solution of multi-dimensional radiative transfer problems on parallel computers.* In: Björstad P. and Luskin M. (eds.) Parallel Solution of PDE, IMA Vol. in Math. and its Appl., **120**, Springer, Berlin Heidelberg New York, 85–96 (2000)

[KM04] Kanschat, G., Meinköhn, E.: *Multi-model preconditioning for radiative transfer problems.* Preprint SFB 359, University of Heidelberg (2004) http://www.sfb359.uni-heidelberg.de/Preprints2004.html

[KPR02] Kurk, J.D., Pentericci, L., Röttgering, H.J.A., Miley, G.K.: *Observations of radio galaxy MRC 1138-262: Merging galaxies embedded in a giant Lyα halo.* In: Henney, W.J., Steffen, W., Raga, A.C., Binette, L. (eds) Emission Lines from Jet Flows. RMxAA (Serie de Conferencias), Vol. **13**, 191–195 (2002)

[Lam65] Lamarsh, J.R.: *Introduction to Nuclear Reactor Theory.* Addison-Wesley Publishing Company, Reading, Massachusett (1965)

[LK74] Larsen, E.W., Keller, J.B.: *Asymptotic solution of neutron transport problems for small scale mean free paths.* J. Math. Phys., **15**, 75–81 (1974)

[LPB83] Larsen, E.W., Pomraning, G.C., Badham, V.C.: *Asymptotic analysis of radiative transfer problems.* J. Quant. Spectrosc. Radiat. Transfer, **29**, 285–310 (1983)

[LMM87] Larsen, E.W., Morel, J.E., Miller, W.F.jun.: *Asymptotic solutions of numerical transport problems in optically thick, diffusive regimes.* J. Comput. Phys., **69**, 283–324 (1987)

[Lar91] Larsen, E.W.: *Transport acceleration methods as two-level multigrid algorithms.* Oper. Theory, Adv. Appl., **51**, 34–47 (1991)

[LR74] LeSaint, P., Raviart, P.-A.: *On a finite element method for solving the neutron transport equation.* In: de Boor (ed.) Mathematical Aspects of Finite Elements in Partial Differential Equations. Academic Press, New York, 89–123 (1974)

[MR02] Meinköhn, E., Richling, S.: *Radiative transfer with finite elements. II. Lyα line transfer in moving media.* Astron. Astrophys., **392**, 827–839 (2002)

[Mei02] Meinköhn, E.: *Modeling Three-Dimensional Radiation Fields in the Early Universe.* Ph.D. Thesis, University of Heidelberg (2002) http://www.iwr.uni-heidelberg.de/sfb359/Preprints2002.html

[Mih78] Mihalas, D.: *Stellar Atmospheres.* W.H. Freeman and Company, Second Edition, San Francisco (1978)

[MW84] Mihalas, D., Weibel-Mihalas, B.: *Foundation of Radiation Hydrodynamics.* Oxford University Press, New York (1984)

[MCK94] Murray, S., Castor, J., Klein, R., McKee, C.: *Accretion disk coronae in high-luminosity systems.* Astrophys. J., **435**, 631–646 (1994)

[Neu90] Neufeld, D.A.: *The transfer of resonance-line radiation in static astrophysical media.* Astrophys. J., **350**, 216–241 (1990)

[Pap75] Papanicolaou, G.C.: *Asymptotic analysis of transport processes.* Bull. Am. Math. Soc., **81**, 330–392 (1975)

[PH98] Park, Y.-S., Hong, S.S.: *Three-dimensional Non-LTE Radiative Transfer of CS in Clumpy Dense Cores.* Astrophys. J., **494**, 605 (1998)

[PSS79] Pozdniakov, L.A., Sobol, I.M., Suniaev, R.A.: *The profile evolution of X-ray spectral lines due to Comptonization - Monte Carlo computations.* Astron. Astrophys., **75**, 214–222 (1979)

[RM01] Richling, S., Meinköhn, E., Kryzhevoi, N., Kanschat, G.: *Radiative transfer with finite elements. I. Basic method and tests.* Astron. Astrophys., **380**, 776–788 (2001)

[SF93] Sleijpen, G.L.G., Fokkema, D.R.: *Bicgstab(L) for linear equations involving unsymmetric matrices with complex spectrum.* Electronic Transactions on Numerical Analysis, Vol. **1**, 11–32 (1993) http://etna.mcs.kent.edu

[SPY95] Sonnhalter, C., Preibisch, T., Yorke, H.: *Frequency dependent radiation transfer in protostellar disks.* Astron. Astrophys., **299**, 545 (1995)

[Spa96] Spaans, M.: *Monte Carlo models of the physical and chemical properties of inhomogeneous interstellar clouds.* Astron. Astrophys., **307**, 271 (1996)

[SL87] Spagna Jr., G.F., Leung, C.M.: *Numerical solution of the radiation transport equation in disk geometry.* J. Quant. Spectrosc. Radiat. Transfer, **37**, 565–580 (1987)

[SAS00] Steidel, C.C., Adelberger, K.L., Sharply, A.E., Pettini, M., Dickinson, M., Giavalisco, M.: *Lyα Imaging of a Proto-Cluster Region at ¡z¿=3.09.* Astrophys. J., **532**, 170–182 (2000)

[SSW91] Stenholm, L.G., Störzer, H., Wehrse, R.: *An efficient method for the solution of 3-D radiative transfer problems.* J. Quant. Spectrosc. Radiat. Transfer, **45**, 47–56 (1991)

[Tur93] Turek, S.: *An efficient solution technique for the radiative transfer equation.* Imp. Comput. Sci. Eng., **5**, No. 3, 201–214 (1993)

[ORM97] van Ojik, R., Röttgering, H.J.A., Miley, G.K., Hunstead, R.W.: *The nature of the extreme kinematics in the extended gas of high redshift radio galaxies.* Astron. Astrophys., **317**, 358–384 (1997)

[Var00] Varga, R.S.: *Matrix Iterative Analysis.* Springer, Berlin Heidelberg (2000)

[WWM04] Warsa, J.S., Wareing, T.A., Morel, J.E.: *Krylov Iterative Methods and the Degraded Effectiveness of Diffusion Synthetic Acceleration for Multidimensional S_n Calculations in Problems with Material Discontinuities.* Nucl. Sci. Eng., **147**, 218–248 (2004)

[WMK99] Wehrse R., Meinköhn E., Kanschat G.: *A review of Heidelberg radiative transfer equation solutions.* In: Stee P. (ed.) Radiative Transfer and Hydrodynamics in Astrophysics. EAS Publication Series, Vol. 5, 13–30 (2002)

[WBW00] Wehrse R., Baschek B., von Waldenfels, W.: *The diffusion of radiation in moving media: I. Basic assumptions and formulae.* Astron. Astrophys., **359**, 780–787 (2000)

[WHS99] Wolf, S., Henning, T., Stecklum, B.: *Multidimensional self-consistent radiative transfer simulations based on the Monte-Carlo method.* Astron. Astrophys., **349**, 839–850 (1999)

[YBL93] Yorke, H., Bodenheimer, P., Laughlin, G.: *The formation of protostellar disks. I - 1 M(solar).* Astrophys. J., **411**, 274–284 (1993)

[ZM02] Zheng, Z., Miralda-Escudé, J.: *Monte Carlo simulation of Lyα scattering and application to damped Lyα systems.* Astrophys. J., **578**, 33–42 (2002)